MANIFOLD LEARNING for IMAGE-BASED GATING of INTRAVASCULAR ULTRASOUND(IVUS) PULLBACK SEQUENCES

by
Gözde Gül İşgüder

Submitted to the Graduate School of Engineering and Natural Sciences
in partial fulfillment of
the requirements for the degree of
Master of Science

Sabancı University
Fall 2010-2011

Manifold Learning for Image-Based Gating of Intravascular Ultrasound(IVUS) Pullback Sequences

APPROVED BY

Assist. Prof. Dr. Gözde ÜNAL ..... (Thesis Supervisor)

Prof. Dr. Aytül ERÇİL .....

Assoc. Prof. Dr. Berrin YANIKOĞLU .....

Assist. Prof. Dr. Müjdat ÇETİN .....

Assist. Prof. Dr. Hakan ERDOĞAN .....

DATE OF APPROVAL: .....

to my family

Acknowledgements

I would like to thank my thesis supervisor Gözde Ünal for her support, encouragement, guidance throughout my thesis as well as her understanding and patience. I would also like to thank her for her great efforts to make this work more valuable, recognizable by giving me a chance to collaborate with other international researchers in the field.

I also would like to thank to our clinical partners Yeditepe Cardiology Department and Ludwig Maximillian University Hospital; our team members Dr. Muzaffer Değertekin, Dr. Ali Kemal Kalkan, Dr. Holger Hetterich and Dr. Johannes Riebber for their valuable guidance and support.

I would like to also thank our project partners at Technical University of Munich: Prof. Nassir Navab, Dr. Martin Groher and Max Baust for their support, guidance and hospitality.

In addition I would like to thank Dr. Carlo Gatta, for kindly sharing in-vitro data with us and Timur Aksoy for providing me a useful program.

I would like to thank Tübitak for providing financial support for my graduate education[1].

My valuable thanks go to all my colleagues at Vision and Pattern Analysis Laboratory, for their great friendship and many thanks to my thesis jury members, Aytül Erçil, Berrin Yanıkoğlu, Müjdat Çetin and Hakan Erdoğan, for having kindly accepted to read and review this thesis.

I owe special thanks to Selcen Gez, Kemal Yaylalı, Cansu Özaltun, Sebastian Marsch and Jürgen Sotke for being there for me for long years. My special thanks to Mehmet Umut Şen, Özben Önhon, Ali Demir, Süheyla Çetin, Serhan Gürmeriç and Andaç Hamamcı for their support and all the good moments we shared together .

Finally, I would like to thank my family Osman, Necla and Erdem İşgüder for their endless support, love and tolerance throughout my life.

[1]This work was supported by Tübitak Grant No:108E162:"Assessment of Fluid Tissue Interaction Using Multi-Modal Image Fusion for Characterization and Progression of Coronary Atherosclerosis", IntenC (Intense Cooperation) Grant, Tübitak-BMBF Germany, 2009-2012.

MANIFOLD LEARNING for IMAGE-BASED GATING of INTRAVASCULAR ULTRASOUND(IVUS) PULLBACK SEQUENCES

Gözde Gül İşgüder

EE, M.Sc. Thesis, 2011

Thesis Supervisor: Gözde ÜNAL

Keywords: Manifold Learning, Classification, IVUS, Intravascular Ultrasound, Image-based gating, ECG gating, Validation

Abstract

Intravascular Ultrasound(IVUS) is an imaging technology which provides cross-sectional images of internal coronary vessel structures. The IVUS frames are acquired by pulling the catheter back with a motor running at a constant speed. However, during the pullback, some artifacts occur due to the beating heart. These artifacts cause inaccurate measurements for total vessel and lumen volume and limitation for further processing. Elimination of these artifacts are possible with an ECG (electrocardiogram) signal, which determines the time interval corresponding to a particular phase of the cardiac cycle. However, using ECG signal requires a special gating unit, which causes loss of important information about the vessel, and furthermore, ECG gating function may not be available in all clinical systems. To address this problem, we propose an image-based gating technique based on manifold learning and a novel weighted ultrasound similarity measure. The parameters for our image-based gating technique were chosen based on the experiments performed on 25 different in-vitro IVUS pullback sequences, which were acquired with the help of a special mechanical instrument that oscillates with given length and frequency. Quantitative tests are performed on 12 different patients, 25 different pullbacks and 100 different longitudinal vessel cuts. In order to validate our method, the results of our method are compared to those of ECG-Gating method. In addition, comparison studies against the results obtained from the state of the art methods available in the literature were carried out to demonstrate the

effectiveness of the proposed method.

INTRAVASKÜLER ULTRASON(IVUS) ÇEKİM DİZİLERİNİN MANİFOLD ÖĞRENMESİ KULLANILARAK GÖRÜNTÜ TABANLI GEÇİTLENMESİ

GÖZDE GÜL İŞGÜDER

EE, Yüksek Lisans Tezi, 2011

Tez Danışmanı: Gözde ÜNAL

Anahtar Kelimeler: manifold öğrenmesi, sınıflandırma, IVUS, intravasküler ultrason, görüntü tabanlı geçitleme, ECG geçitlemesi, validasyon

Özet

İntravasküler Ultrason(IVUS) iç koroner damarların kros-kesitlerinin görüntülenmesine olanak sağlayan bir görüntüleme tekniğidir. IVUS çerçeveleri, sabit hızlı bir motor yardımıyla kateterin damardan geriye doğru çekilmesiyle elde edilmektedir. Ancak, bu geriçekilme esnasında kalbin atmasından ötürü görüntü üzerinde istenmeyen bozulmalar meydana gelmektedir. Bu bozulmalar damar ve iç damar hacim ölçümlerini yanıltmakta ve işlemlerin devamlılığını sınırlandırmaktadır. Kardiyo sisteminin bulunduğu faza ait olan zaman aralığını tespit edebilen ECG(elektrokardiyogram) sinyaliyle bu bozulmaların önlenmesi mümkündür. Ancak, ECG sinyalinin kullanılabilmesi için özel bir geçitleme ünitesine ihtiyaç vardır ve bu ünitenin kullanımı damarla ilgili önemli bilgilerin kaybolmasına yol açabileceği gibi, her klinikte mevcut olmayabilir. Bu problemi çözmek üzere manifold öğrenmesine ve yeni bir ağırlıklı ultrason benzerlik ölçütüne dayalı bir görüntü tabanlı geçitleme tekniği önerilmiştir. Görüntü tabanlı geçitleme tekniğimizin parametreleri, verilen uzunluk ve frekansla salınabilen IVUS çekimlerini gerçekleştirebilen özel bir enstrümanla alınan 25 farklı veri kümesi üzerinde deneyler yapılarak belirlenmiştir.

11 değişik hasta, 22 değişik IVUS çekimi ve 88 değişik damar kesiti üzerinde nicel testler uygulanmıştır. Metodun geçerliliğini test etmek amacıyla metodun sonuçları, ECG geçitlemesinin sonuçlarıyla karşılaştırılmıştır. Buna ek olarak, literatürde mevcut olan diğer görüntü tabanlı geçitleme yöntemleriyle karşılaştırmalar yapılarak, önerilen metodun verimliliği gösterilmiştir.

Table of Contents

List of Figures

List of Tables

Chapter 1

Introduction

1.1 Motivation

Intravascular Ultrasound is invasive catheter-based imaging technology that yields a high resolution, real-time cross-sectional view of the blood vessels from inside-out. The cross-sectional images are acquired by pulling a catheter back with a motor running at a previously defined constant speed, which is referred as a pullback. An illustration of cross-sectional and longitudinal views is shown in Fig. 1.1.

Since IVUS modality provides a very detailed information about the internal vessel structures, it is a unique tool for the diagnostics of coronary artery diseases(CAD) and plaque characterization. For diagnosis and assessment of the disease, accurate measurements of the total vessel and the lumen volume in the suspicious lesion areas are crucial. However, quality of the IVUS evaluations, and accuracy of the measurements deteriorate due to artifacts caused by heart movement during a pullback [14]. The most obvious artifact is the back and forth movement of the catheter in the vessel longitudinal direction due to the periodical change in the blood flow while the heart muscles are contracting and expanding. As the transducer moves back and forth, it passes through the same locations of the vessel multiple times; thus it oversamples the vessel. This means sampling unnecessary information which leads to computational inefficiency for further processing. Furthermore, due to the heart movement, the longitudinal cut of the vessel has a saw-toothed appearance(see Fig. 1.2) which makes the segmentation of the vessel even harder. Another artifact caused by the cardiac cycle is the change of the vessel morphology due to the varying blood pressure during the cycle. The change in the morphology leads to the variations in the lumen area observed at different cardiac phases (systole,diastole). In [14],[4], it is stated that measured lumen and vessel volumes in non-gated image sets are significantly larger than normal

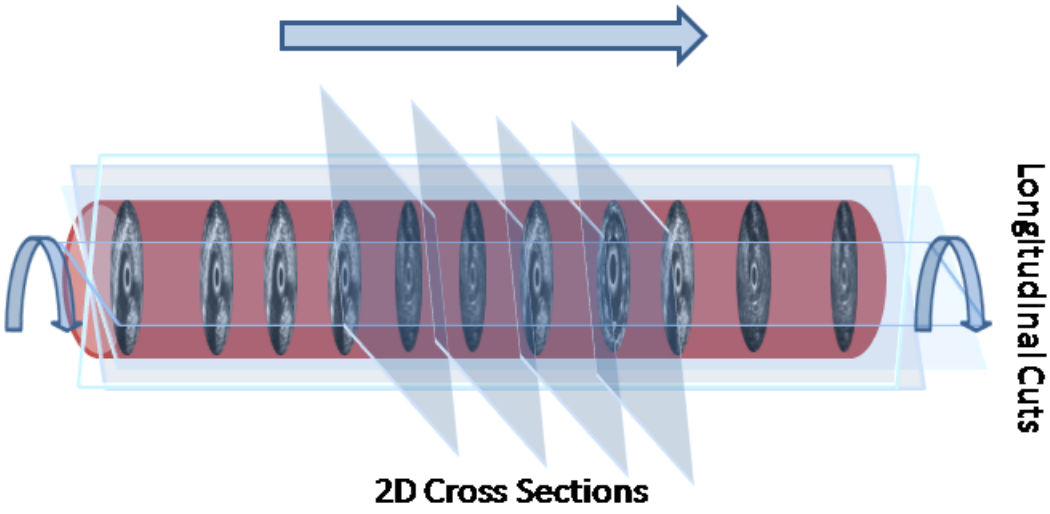

Figure 1.1: Illustration of cross-sectional and longitudinal view of the blood vessels. Longitudinal views are obtained by cutting the vessel in longitudinal direction with different angles and 2D cross-sectional views are obtained by cutting the vessel in orthogonal direction.

and the choice of the suitable phase is still a question. A way to account for the problems above is introducing an electrocardiogram (ECG) signal, which is capable of giving information about the heart's current physical status. By utilising the ECG signal, heart and IVUS transducer are synchronized so as to capture the frames only near the predetermined fraction of the RR-interval [14]. An example of RR-Interval is shown in Fig. 1.10 and explained in Section 1.3.1. However online-ECG gating requires an ECG unit, which often increases the image acquisition time and which may not be always available to the physician.

In this work, we introduce a robust image-based gating method based on manifold learning. By designing this method, our overall aim is to retain only the necessary information about the vessel, (the frames at a particular fraction of the RR-interval), which will adequately provide accurate lumen volume measurements and vessel length; at the same time will avoid loss of important plaque information in the lesion areas.

In the following sections, more detailed information on the medical background is given to introduce the subject more clearly and with more depth. In Section 1.1.1, Intravascular Ultrasound(IVUS) properties and how it is acquired is briefly explained. In Section 1.2, the artifacts that occur during the acquisition is explained in details. In Section 1.3, the hardware

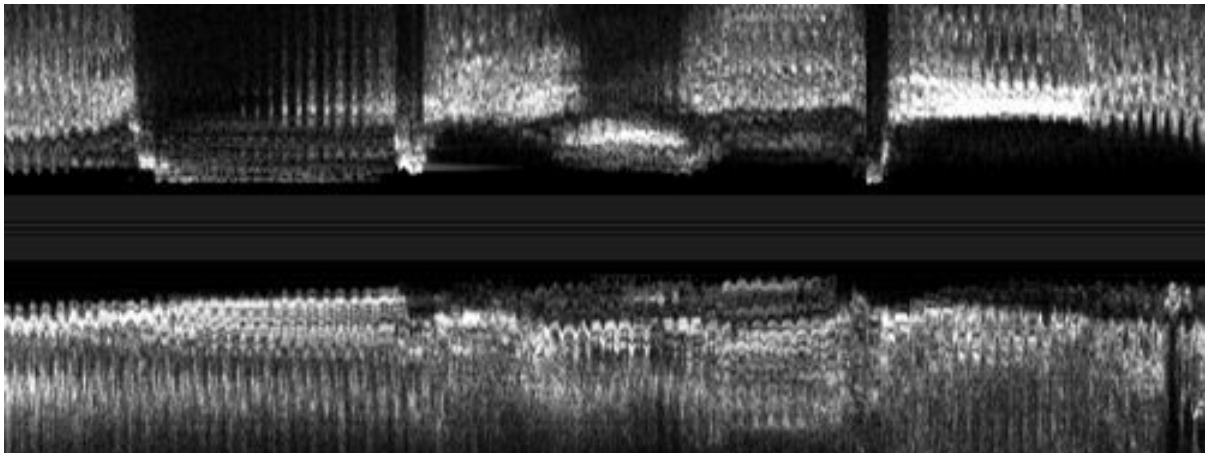

Figure 1.2: Longitudinal cut view of a nongated IVUS pullback shows a jagged character.

solution ECG(ElectroCardiogram) Gating and the previous software solutions for the problem that exist in the literature are introduced. After that in Section 1.4, contributions of this thesis are itemized. Finally in the last section, outline of the thesis is given.

A preliminary version of thesis work is published in [15], and presented at International Workshop on Medical Imaging and Augmented Reality 2010. This work is a substantially expanded and revised version of [15].

1.1.1 Intravascular Ultrasound (IVUS)

Coronary Artery disease(CAD) arises when the coronary arteries become clogged with fatty deposits called plaque(See Fig. 1.3). Regarding 2006 Statistics done by American Heart Association, coronary heart disease caused 425,425 deaths and is the single leading cause of death in America today. (Other mortality: total cancer 559,888; accidents 121,599; HIV (AIDS) 12,113.)

Intravascular ultrasound (IVUS), a diagnostic imaging technique, offers a unique view of the morphology of the arterial plaque and displays the morphological and histological properties of a cross-section of the vessel. IVUS is an important intravascular imaging technique, since it provides us with detailed information about the lumen, plaques and plaque types. It allows the application of ultrasound technology to see from inside blood vessels out through the surrounding blood column, visualizing inside of the blood vessel wall tissue in living individuals. Thus, these properties make IVUS unique, in diagnosis of coronary artery diseases that are caused by the arterial plaques. In Fig. 1.4, IVUS images are overlaid with segmentation contours obtained by Unal et al [2]). On the left side, the popular view of IVUS that are mostly used by cardiologists

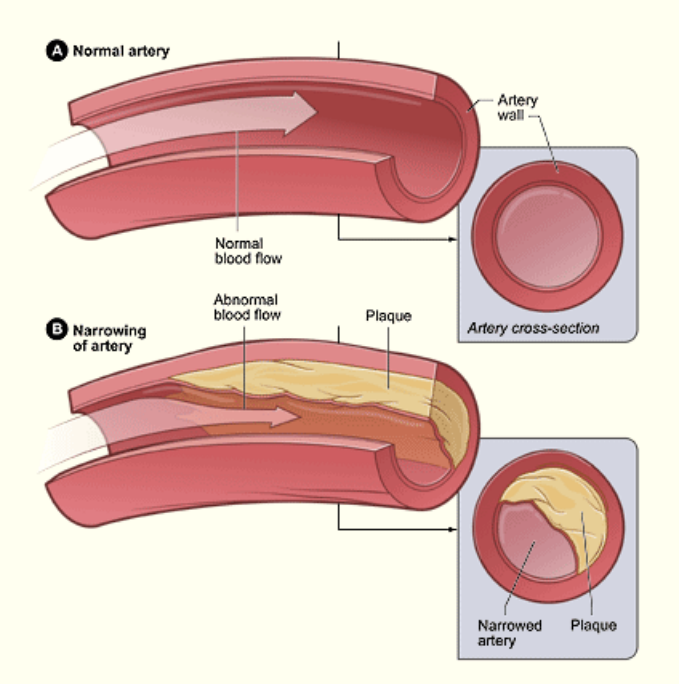

Figure 1.3: Vessel with CAD (Adopted from [1]).

are shown, while on the right side, the same image in polar domain is shown. The area inside the yellow contour is referred as lumen. It is the inner open space of the vessel, wherein blood flows. The wall that is shown with cyan contour is called media and represents the outer vessel wall. The arterial plaques that cause coronary artery diseases lie in the area separated by lumen and media-adventitia contours. In order to diagnose CAD, the cardiologists need accurate information about the lumen volume and plaque configuration between the lumen and media-adventitia contours.

Acquisition

Intravascular ultrasound (IVUS) is acquired using a specially designed catheter with a miniaturized ultrasound probe attached to the distal end of the catheter. The proximal end of the catheter is attached to computerized ultrasound equipment [16]. In Fig. 1.5, an illustration of IVUS acquisition is shown.

First step is inserting the guidewire into the part of the coronary vessel that is to be imaged(shown in Fig. 1.5 (1)) from outside the body. The guidewire has a very soft and pliable tip and has a certain length around 200 cm. During the insertion of the guide-wire, the physician simultaneously checks the angiogram of the subject vessel in order to decide which direction to steer the wire.

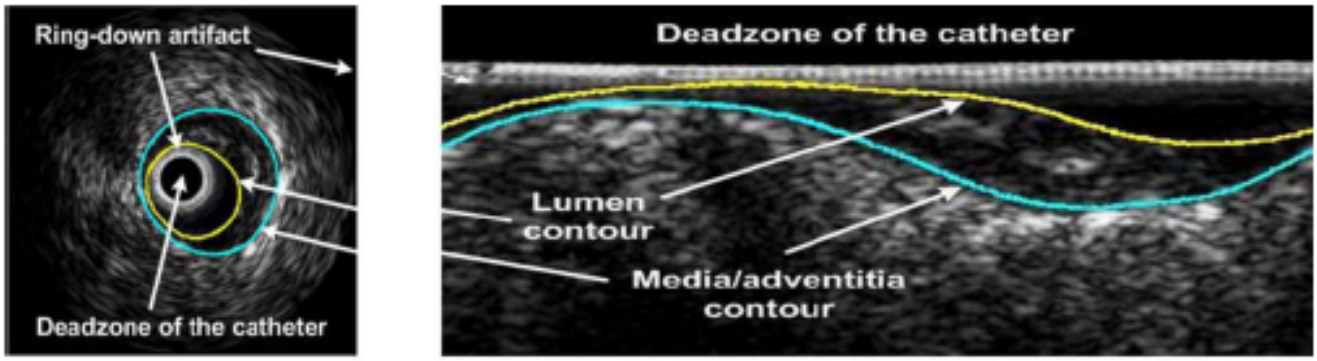

Figure 1.4: a)IVUS display domain b)IVUS polar domain(taken from [2]).

Secondly, the ultrasound catheter tip is slid in over the guidewire so that its tip is positioned to be at the farthest away position to be imaged. Also, the other end of the catheter is connected to the motor unit referred as pullback device.

Finally the ultrasound catheter tip is slid backwards, under motorized control usually at a speed of 0.5 mm/s as shown in Fig. 1.5 (3). This whole process is referred as a pullback.

1.2 Artifacts

Two main artifacts occur during the acquisition of the IVUS due to heart movement. Those two artifacts and their complications are discussed in the following subsections.

1.2.1 Cardiac Motion and Vessel Morphology Change

A 3D reconstruction of sample coronary vessels in different phases of the cardiac cycle is shown in Fig. 1.6. The area shadowed with red, shows the dramatic change that the coronary arteries go through during the expansion(diastole) and contraction(systole).

This change is also observable in IVUS images as shown in Fig. 1.7. The change in the morphology leads to the variations in the lumen area observed at different cardiac phases(systole,diastole). Lumen is 20% larger in Diastole(expansion) phase [14],[4] and calcified Plaque Area is larger in systole phase [4].

Due to the fact that lumen volume and plaque configuration differ in different phases of the cardiac cycle and IVUS images are acquired at all phases of the cardiac cycle; it is critical to

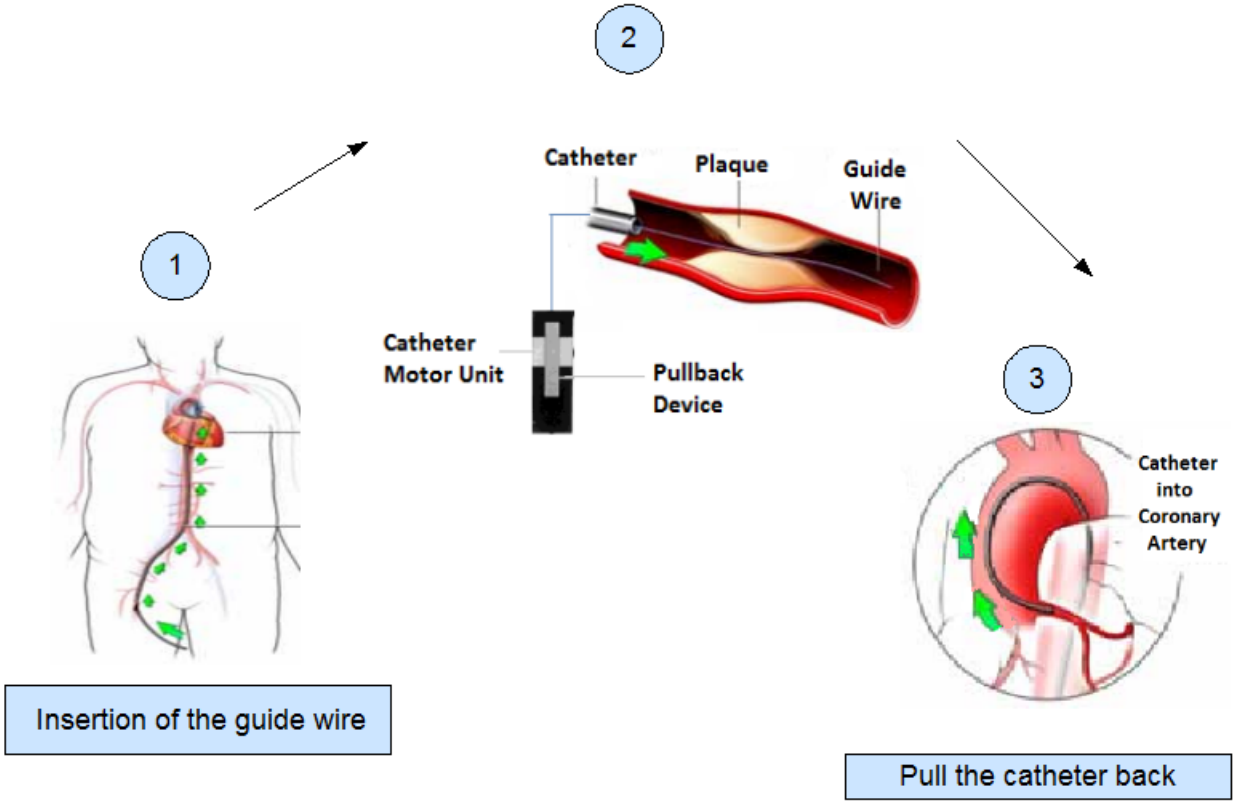

Figure 1.5: IVUS acquisition steps.

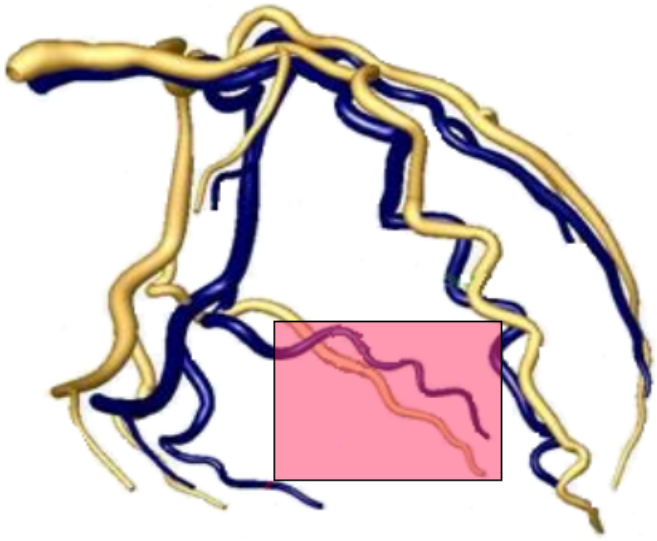

Figure 1.6: Yellow shows the position of the coronary arteries during expansion(diastole), blue shows the position of the coronary arteries during contraction(systole)(adopted from [3]).

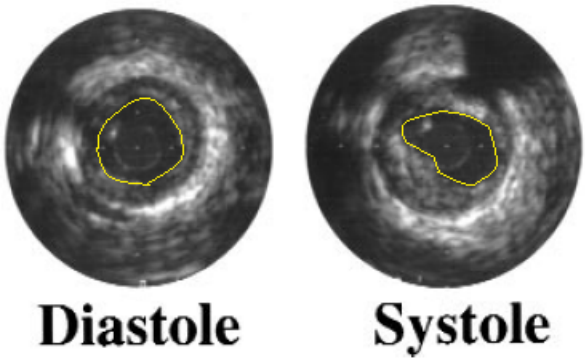

Figure 1.7: Lumen Area Difference between systole and diastole (taken from [4]).

evaluate IVUS images taken at the same phase for correct diagnosis.

1.2.2 Catheter Motion

As stated in Section 1.1, the most obvious artifact is the back and forth movement of the catheter in the vessel longitudinal direction due to the periodical change in the blood flow while the heart muscles are contracting and expanding. In [4], the authors observe that the IVUS transducers within coronary vessels have a longitudinal movement of average 1.50 ± 0.80 mm during each cardiac cycle. In Fig. 1.8, the black arrows illustrate the back and forth motion of the catheter, where the thick blue arrow shows the pullback direction.

Due to the back and forth motion of the catheter, it is not possible to estimate the position of the catheter tip from the parameters of the IVUS pullback, hence the exact coronary arterial cross-section that is being imaged at a given time. Thus, it causes an important obstacle in extraction of true 3D geometry of the vessel subject to the pullback.

Moreover, as the catheter moves along, it samples the same sections of the vessel multiple times, thus gives us an oversampled data. Further analysis of the oversampled data is time-consuming and provides no extra valuable information, therefore should be avoided.

1.3 Literature Review

The problems that were discussed in Section 1.2 can be solved by choosing the "stable frames" from the pullback where the heart is almost motionless. However, even in medicine literature, the most stable phase of the heart is still not exactly defined, and also it is still an issue of debate

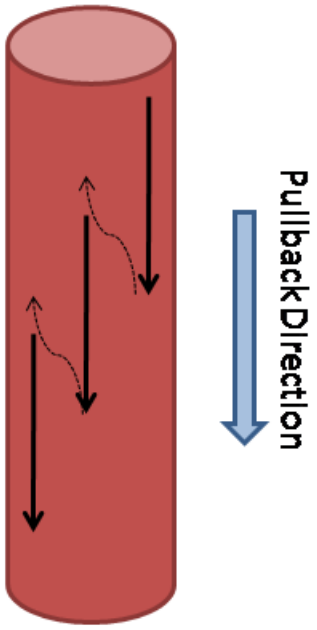

Figure 1.8: Rough Illustration of Catheter Movement, where solid lines show the forth movement and dashed lines illustrate the back movement of the catheter.

on which phase gives the best representation of the arteries in IVUS images[14]. However, the problem can be partially solved by choosing a group of frames that are acquired at the same cardiac phase. This choosing process is called "gating" and illustrated in Fig. 1.9. In the figure a) the original pullback without gating is shown and in b) the frames that belong to the same cardiac phase are shown with dashed lines. Finally in c) the pullback is reconstructed by stacking up the frames that are chosen in b). It can be observed that the resolution of the reconstructed view is much lower than the ungated view, however they appear very similar. It is because that the chosen amount of frames can adequately represent the vessel as well as all the frames in the pullback.

There are two possible methods of gating: First one is a hardware solution, called ECG Gating, and is explained in section 1.3.1; second one is a software solution based only on the image information, that is proposed in this thesis and is discussed in section 1.3.2.

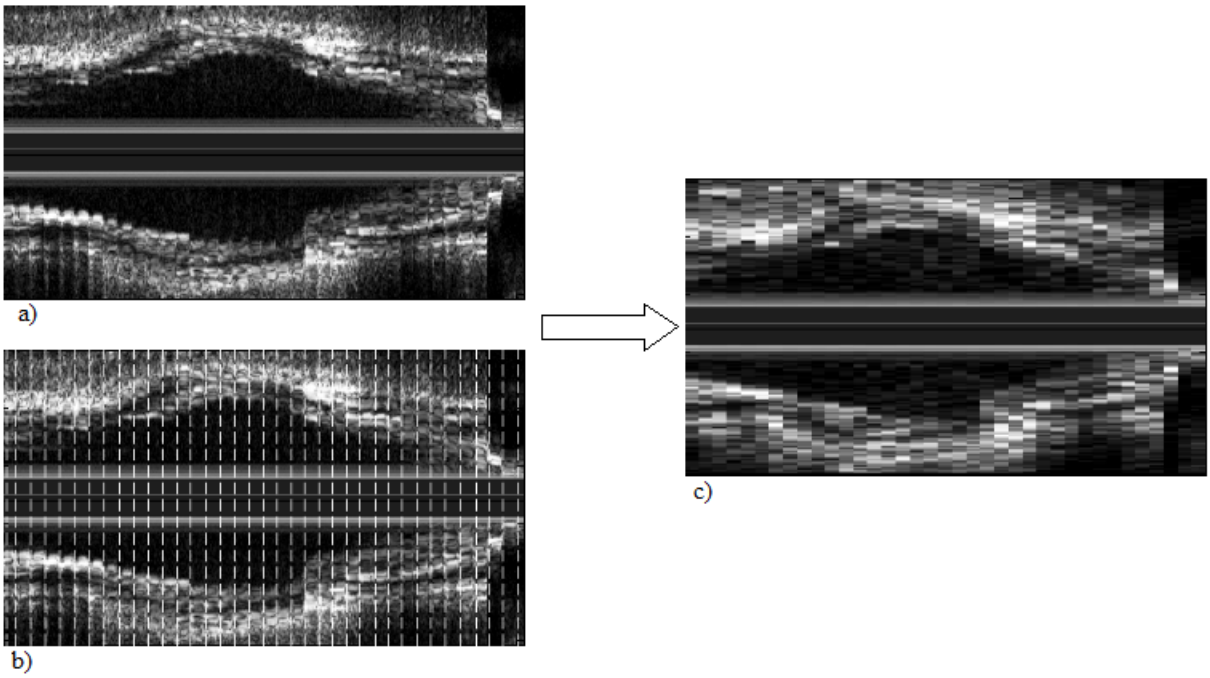

Figure 1.9: Illustration of gating idea. a) Ungated pullback b)Dashed lines: The frames acquired in the same cardiac phase, c) Reconstruction of the pullback.

1.3.1 ECG(Electrocardiogram) Gating

Electrocardiography (ECG, or EKG [from the German Elektrokardiogramm]) is a transthoracic interpretation of the electrical activity of the heart over time captured and externally recorded by skin electrodes[17]. In Fig. 1.10, an examplary signal that is produced by the electrocardiography device is shown. The signal is referred as an R-Wave.

The acquisition procedure that was explained in Section 1.1.1, slightly changes if ECG gating will be incorporated. As can be seen in Fig. 1.11, the special gating unit is connected to the IVUS machine, in order to sample at a certain fraction of the RR interval.

ECG Gating has some advantages such as being accurate and not requiring a post processing, as well as disadvantages such as not being available in all clinics, increasing the acquisition time and causing loss of important information about the plaques[14].

1.3.2 Previous Solutions

In [18], a method for classification of the IVUS frames as end-diastolic and not end-diastolic is presented. As preprocessing, important image characteristics such as edges are enhanced,

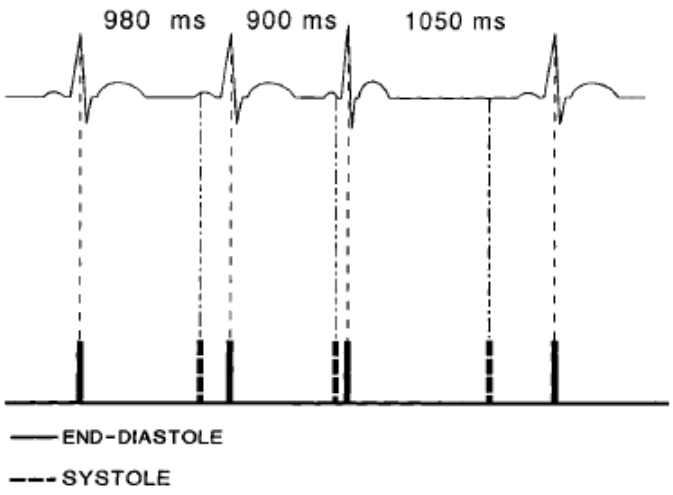

Figure 1.10: RR Interval.

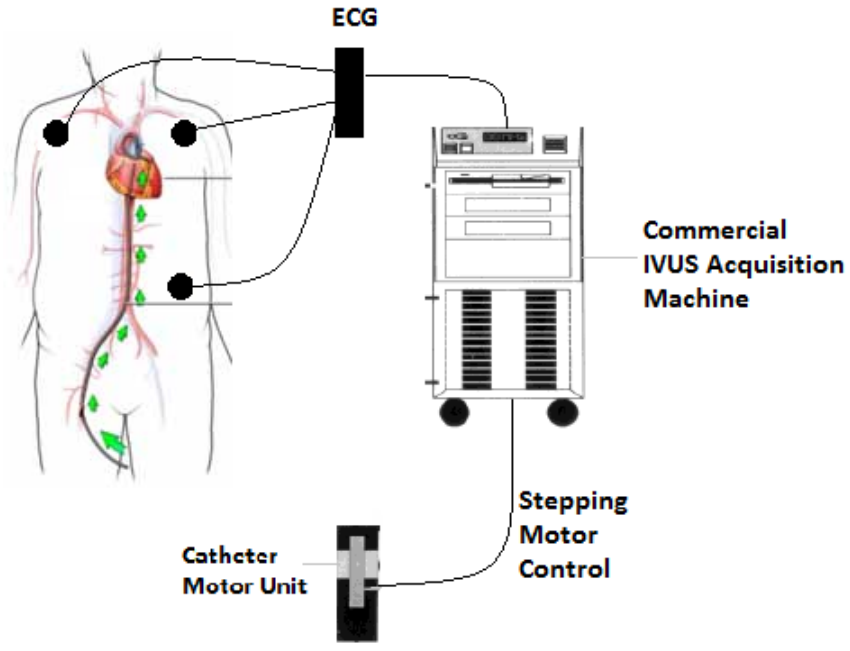

Figure 1.11: ECG Gating Procedure.

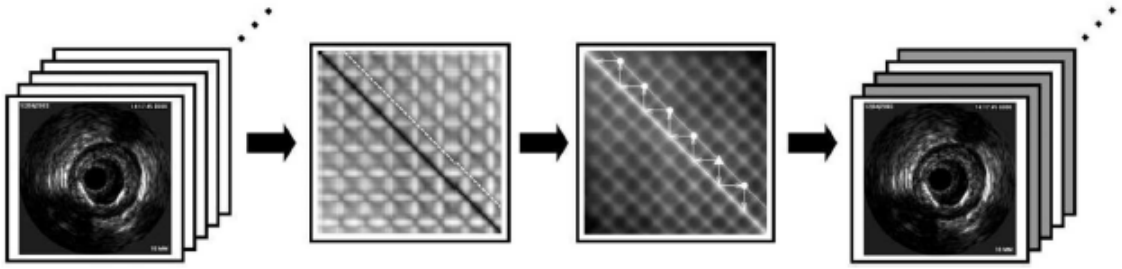

Figure 1.12: Flowchart of the gating process. Left to right: ungated pullback; D matrix and the shortest path; $\hat{D}$ matrix and chosen frames on diagonals; gated pullback.

different feature vectors based on spatial and frequency characteristics of the images are defined, and finally a nearest neighbor search based on the Euclidean distance between the feature vectors is used to classify the frames.

In [11], the authors present a method to retrieve the cardiac phase by examining a circular region of interest in all images. They define Average Intensity(AI) and Absolute Intensity Difference(AID) as two different features for each frame. Those signals are extracted from each frame and then is filtered with a Butterworth bandpass filter for noise elimination purposes. In their work, only the filtered signals are shown and the central frequency is extracted. Gating is not actually performed on the signal.

In [19],[13], an image-based gating algorithm is proposed where a Dissimilarity Matrix(D) based on the Normalized Cross Correlation (NCC) is built between each 2-tuples of the pullback. The matrix is forced to have 0-values on diagonals, also the matrix is forced to be positive and symmetric. After that, D is filtered with an X-shaped inverted Gaussian kernel, which highlights the frames with high similarity, and is called $\hat{D}$. Then a dynamic programming technique is incorporated in order to find the shortest path along the matrix D by tracing only down and right, starting from the right diagonal neighbor of the main diagonal. Finally a simple tracing algorithm is introduced to find the highest local maxima along the shortest path on the diagonals of $\hat{D}$, that represents the optimal gating frames. The whole process is shown in Fig. 1.12.

In [20], the authors use a similar technique to [19], by building the dissimilarity matrix D based on the image descriptors which are defined based on Gabor patches. A 1D signal is extracted from D, which defines the similarities between the frames and finally a local minimum search over the 1D signal is performed to obtain the best frames.

In [10], the authors define a motion blur signal, which is based on the vertical derivative of the IVUS images in polar domain. The method is based on the idea that a motion blur effect proportional to the speed of the tissue movement occurs due to tissue displacement. Then the extracted signal is filtered with Butterworth high pass filter for noise elimination purposes. Only in-vitro experiments are done, where in-vitro data was acquired with the help of a special mechanical device that simulates the heart beat with a given constant length of oscillation and frequency.

1.4 Contributions

The previous work on gating of IVUS pullback sequences in the absence of ECG gating device, indicate that the important point is to be able to extract an R-Wave like 1D Signal or a signature using image intensity properties from IVUS pullback frames. In this thesis, our hypothesis is that using a nonlinear dimensionality reduction technique, we could transform the IVUS image space into a low-dimensional space on which one can cluster the images that are similar in some defined sense, and extract a 1D signal from which a stable image frame can be selected, hence gating is achieved. We present the required mathematical methodology, and the necessary experimental validation in our attempt to prove that the proposed technique improves the image-based gating of IVUS pullback sequences. Our contributions in this thesis can be summarized as follows. We have:

- Adopted and applied the manifold learning framework to our problem of image-based gating of IVUS pullbacks;
- Proposed a new similarity measure for ultrasound images and showed that the new measure is superior to others in IVUS pullbacks;
- Proposed a new validation method that approximates lumen volume measurements by employing lumen area measurements for different longitudinal vessel cuts calculated in different angles;
- Presented extensive comparison results among the existing image-based IVUS gating algorithms in the literature.

1.5 Outline

This thesis is organized as five chapters including the Introduction chapter. In Chapter 2, a background on current linear and nonlinear dimensionality reduction techniques are given. Proposed image-based gating algorithm based on manifold learning is given in Section 3. The experimental results are provided and discussed in Chapter 4. In the last chapter, the conclusions and future work are expressed.

Chapter 2

Dimensionality Reduction Techniques

In this chapter, well-known dimensionality reduction techniques that are most commonly used for medical imaging problems are described. In the first section, linear dimensionality reduction techniques are presented. In the second section of the chapter, nonlinear reduction techniques are introduced.

Together with the recent rapid technological development in the medical imaging field, more complex tools for imaging are introduced every day. These tools provide the doctors more advanced, high-resolution, detailed images and thus a higher rate of diagnosis, planning and evaluation. However, those high-dimensional, complex data yield time-consuming, inefficient further computations, difficulty for extracting the underlying relation between the images and visualization of the general structure. In addition to that, in many cases, not all the measured variables are important for understanding the underlying phenomena of interest. Other than these, it is difficult to extract statistical information from high dimensional data.

All the reasons stated above, give the researchers the motivation for finding ways of representing the high dimensional data in a low dimensional space. This process is referred as "dimensionality reduction". In mathematical terms:

Given a set of k points $x_1, ..., x_k$ in $\mathbb{R}^d$, where k is the number of samples and d is the dimension of the data; find another set of k points $y_1, ..., y_k$ in $\mathbb{R}^m$, where $m \ll d$.

Dimensionality reduction is a helpful tool for multidimensional observations, that is applied prior to any analysis or processing application such as clustering and classification. A variety of dimensionality reduction techniques have been proposed in the literature and they can be broadly classified into two groups as linear and nonlinear methods. Dimensionality reduction techniques do not just reduce the dimension, but also preserve the structure of the high-dimensional data

after the projection of the high dimensional data onto a low dimensional space with minimum loss of information.

2.1 Linear Dimensionality Reduction Techniques

If the mapping of the high dimensional data is linear, the technique is called "linear dimensionality reduction". The general procedure for all linear dimensionality reduction is the same. First of all, a mxd transformation matrix $\boldsymbol{W} = [\boldsymbol{w}_1, \boldsymbol{w}_2, ..., \boldsymbol{w}_m]^T$, such that $\boldsymbol{f} = \boldsymbol{W}\boldsymbol{x}$ is created. Our aim is to find d-dimensional column vectors(basis vectors) $\boldsymbol{w}_i$'s that will constitute the rows of the transformation matrix $\boldsymbol{W}$. Finally input data $\boldsymbol{x}$ is projected onto these basis by multiplying with $\boldsymbol{W}$.

$$\boldsymbol{W} = \begin{bmatrix} \boldsymbol{w}_1^T \\ \boldsymbol{w}_2^T \\ . \\ . \\ . \\ \boldsymbol{w}_m^T \end{bmatrix}.$$

Since we assume that the rows of $\boldsymbol{W}$ are orthogonal, the coefficients f_i's that represent $\boldsymbol{x}$ as a linear combination of basis elements $\boldsymbol{w}_i$'s can be found. We can calculate the approximation of $\boldsymbol{x}$, which is represented with $\hat{\boldsymbol{x}}$, by using basis coefficients, as following:

$$\hat{\boldsymbol{x}} \cong \sum_{i=1}^{m} f_i \boldsymbol{w}_i. \tag{2.1}$$

2.1.1 Principal Component Analysis(PCA)

The criterion that Principal component analysis (PCA) maximizes is the variance of the sample points [12]. It tries to spread the sample points as far as possible so that the differences between the sample points become obvious. PCA provides an orthonormal basis for the best subspace that gives minimum least squared error on samples. First principal component is in the direction of the maximum variance in the data and the second component is in the direction of the second maximum variance in the data and so on. In dimension reduction by using PCA, characteristics of the data that contribute most to its variance are kept by keeping lower-order

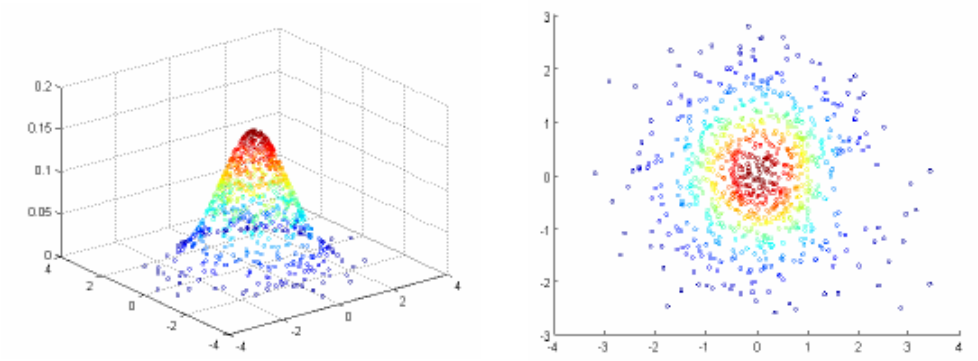

(a) (b)

Figure 2.1: (a)3D Gaussian Data (b) 2D Projection of the data in (a) projected by PCA.

principal components. So, by using less amount of information, most of the variance of the data is captured. The rows of the transformation matrix, $\boldsymbol{W}$ are selected as the eigenvectors that corresponds to the m highest eigenvalues of the scatter matrix $\boldsymbol{S}$ are selected,

$$\boldsymbol{S} = \sum_{k=1}^{n} (\boldsymbol{x}_k - \boldsymbol{\mu})(\boldsymbol{x}_k - \boldsymbol{\mu})^T, \tag{2.2}$$

where $\boldsymbol{x}_k$ represents the k^{th} sample and μ is the sample mean.

A toy example for PCA is shown in Fig. 2.1. It can be noticed that the calculated basis vectors by PCA nicely represent the direction of the maximum variances.

PCA explains variance but is very sensitive to outliers [21]. Even a little amount of outliers may ruin the results of PCA, thus it is usually used for visualization in order to have a rough idea about the input. The results can be improved by using more robust distances, such as Mahalanobis distance.

2.1.2 Normalized Principal Component Analysis(NPCA)

Normalized PCA is introduced for generalization purposes of regular PCA. In regular PCA, an unweighted sum of the squared distances is maximized. The idea in normalized PCA is to place samples from different class further from each other in the projected space by introducing a weighting scheme. In [5], it is shown that PCA maximizes the sum of all squared pairwise distances between the projected vectors. Hence solving the maximization of this sum in the projected space yields to the same result with regular PCA.

Let's show the sum of squared distances in the projected space as $\sum_{i<j}(\text{dist}_{ij}^m)^2$ where dist_{ij}^m is the distance between elements i and j in the projected space, then we seek the projection that

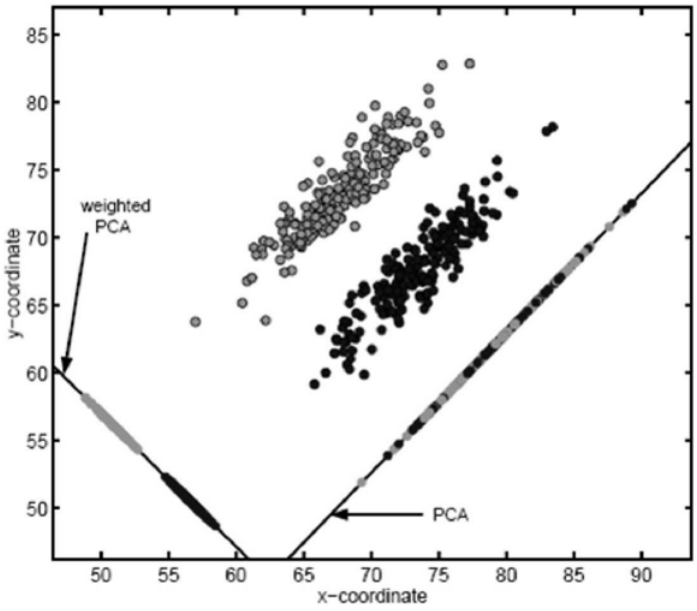

Figure 2.2: PCA vs Normalized PCA (taken from [5]).

maximizes the weighted sum:

$$\sum_{i<j} d_{ij}(\text{dist}_{ij}^{m})^2. \tag{2.3}$$

d_{ij}'s are called pairwise dissimilarities, so by defining these pairwise dissimilarities, we can place elements from different classes further from each other. If we set $d_{ij} = 1$, we get the same result with regular PCA. In [5], pairwise dissimilarities are introduced as $d_{ij} = \frac{1}{\text{dist}_{ij}}$ where dist_{ij} is the distance between elements i and j from different classes, in the original space. The solution of the maximization problem in Eq. 2.3 leads to the the generalized eigenvectors that corresponds to the m highest eigenvalues of $\boldsymbol{X}^T\boldsymbol{L}^d\boldsymbol{X}$ or $\boldsymbol{X}^T\boldsymbol{X}$, where $\boldsymbol{L}^d$ is a Laplacian matrix derived by pairwise dissimilarities and $\boldsymbol{X}$ is data matrix (one sample in each row). It is shown that the matrices $\boldsymbol{X}^T\boldsymbol{L}^d\boldsymbol{X}$ and the covariance matrix $\boldsymbol{X}^T\boldsymbol{X}$ are identical up to multiplication by a positive constant[5]. Please see [5] for proof of the maximization problem stated in Eq. 2.3. By selecting pairwise dissimilarities as inversely proportional to their distances in the original space, on the overall criterion we emphasize the elements that are close to each other and give less importance to the elements that are already apart. If elements i and j belong to same class, d_{ij} can be set to 0, which means we are not interested in separating elements within the same class. As a conclusion, normalized PCA becomes able to discriminate classes in the projected space where PCA may fail as it does not take class information into account.

In the Figure 2.2, a 2-D dataset is projected to 1-D by using both PCA and Normalized PCA

into two different directions. In PCA case, PCA fails to discriminate classes in the projected space. However, by the introduction of pairwise dissimilarities Normalized PCA is able to capture the class decomposition.

2.1.3 Multidimensional Scaling(MDS)

Multidimensional Scaling places the high dimensional points on a low dimensional map, such that the pairwise distances d_{ij} for all $i, j = 1, ..N$ where N is the number of samples, are preserved [22]. The distance can be chosen amongst the popular metrics such as Euclidean distance (L_2 norm) or Manhattan distance (L_1 norm). In mathematical terms;

Given n items $\{x_i\}_{i=1}^n \in R^d$ and a symmetric distance matrix $\triangle = \delta_{ij}, i, j = 1, ..., N$, the result of a m-dimensional MDS will be set of points $\{y_i\}_{i=1}^n \in R^m$ such that the distances $d_{ij} = d(y_i, y_j)$ are as close as possible to a function f of the corresponding proximities $f(\delta_{ij})$ [23], where $\delta_{ij} = d(x_i, x_j)$. The following function is minimized.

$$\hat{f} = \underset{f}{\operatorname{argmin}} \sqrt{\frac{\sum_{i,j}[f(\delta_{ij} - d_{ij})]^2}{scalefactor}} \tag{2.4}$$

where the scale factor is usually based on $\sum_{i,j}[f(\delta_{ij})]^2$ or on $\sum_{i,j} d_{ij}^2$.

Finally the best projections y_is are determined as follows:

$$\hat{Y} = \underset{Y}{\operatorname{argmin}} \hat{f} \tag{2.5}$$

If distance measure is chosen as the Euclidean distance and f is identity in Eqn. 2.4, the procedure is the same as PCA, however the computation time is much longer. In Figure 2.3, the approximated travel distances between cities after applying MDS are shown with the real world map(taken from [21]). It can be seen that the distances are preserved as well as possible.

2.2 Nonlinear Dimensionality Reduction Techniques

Even though most of the linear dimensionality reduction methods are easy to implement and efficient, they are not suitable for the real world problems, which contain nonlinearities. As an example, take a face recognition application, where a face is represented as a two-dimensional, 100x100 image. Thus, we can say that each face is is a point in a 10,000 dimensions. As we take pictures of a person slowly rotating his/her head from left to right; the sequence of images

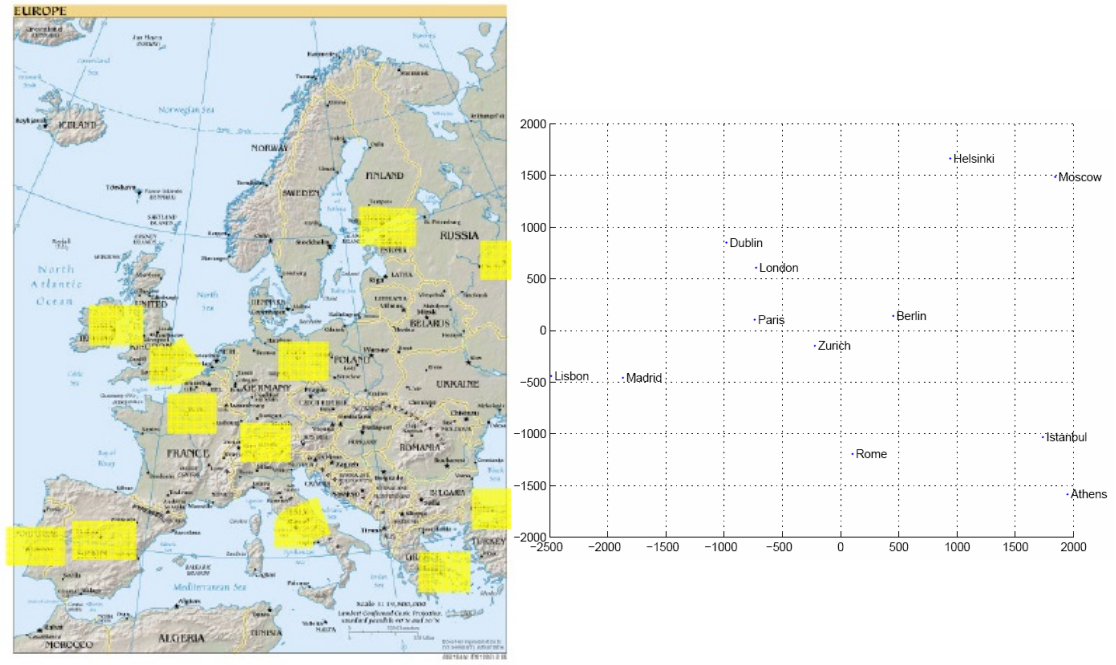

(a) (b)

Figure 2.3: (a)Real World Map (b)Projection of real world distances by MDS.

we capture follows a trajectory in the 10,000-dimensional space and this is not linear[21]. These trajectories define a manifold in the 10,000-dimensional space, which we want to model. Thus, nonlinear dimensionality reduction techniques(NLDR) are introduced to generate better results where linear methods break down at the nonlinearities like in the application explained above. Linear approximations for the nonlinear problem is the essence of the NLDR's. Most of the NLDR's are based on k nearest neighbor(knn) graphs, where the connectedness between pairs are defined to estimate local properties of the manifold. Then the best global mapping that preserves the local distances is calculated.

2.2.1 Isometric Feature Mapping (Isomap)

In the previous section(2.1.1), PCA is discussed. In PCA, Euclidean distances were used as a measure of similarity between the sample points. However, in nonlinear cases Euclidean distances do not give us the right distance between two samples. A typical example of a nonlinear data, swissroll, and the two different distances between two sample points are given in Fig. 2.5. As can be seen Fig. 2.5 b) gives more reasonable explanation than 2.5 a) for the distances between two sample points. That distance is referred as geodesic distance. Geodesic distance preserves

locality.

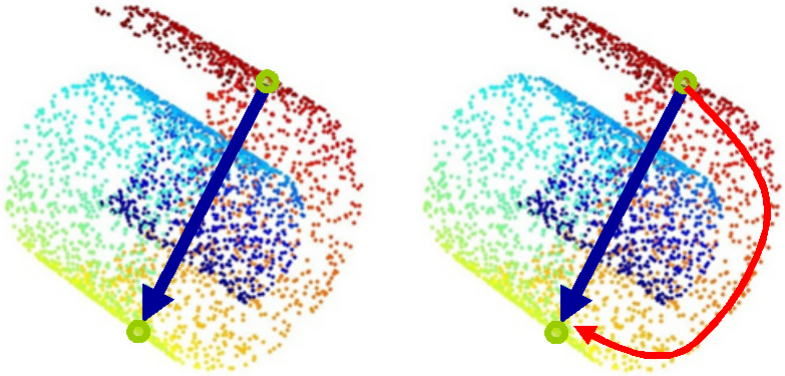

(a) (b)

Figure 2.4: (a)Euclidean Distance between two selected points(blue line)(b)Geodesic Distance between two selected points(red line)

In Isomap [6], geodesic distances between all pairs of data points are used. Since the data is assumed to be locally linear, the Euclidean distances between the neighboring points can be used. After the Euclidean distances between the neighboring points are calculated, the geodesic distance between the non-neighbor points can be approximated by summing up the Euclidean distances of the in-between points.

In order to employ the geodesic distances $d_G(i,j)$ between x_i and x_j in the calculation, Isomap defines a weighted neighborhood graph $G =< X, E >$, where the nodes correspond to N points: $X = \{x_1, x_2, ..., x_N\}$ and edges E correspond to the weights between each pair of nodes. The weights between each pair is defined as the shortest path between those nodes. Dynamic programming techniques such as Djikstra[24] can be used to calculate the shortest path between the nodes. In mathematical terms, following is done:

Initialize, $d_G(i,j) = d_X(i,f)$ if connected, ∞ otherwise. For each $i = 1, 2, ..., N$,
replace $d_G(i,j) = min(d_G(i,j), d_G(i,k) + d_G(k,j))$.

In Fig. 2.6, the steps of calculating the geodesic distances are shown. In A, the nonlinear data is given as a swissroll. In B, the neighborhood graph is shown and in C, the geodesic distance between two sample points(in red) and the true shortest distance(in blue) is shown. In Fig. 2.7, some results from a real world problem is shown. As can be seen, two chosen eigenvectors explain the variation in light condition and up-down pose of the image compactly and in a continuous manner.

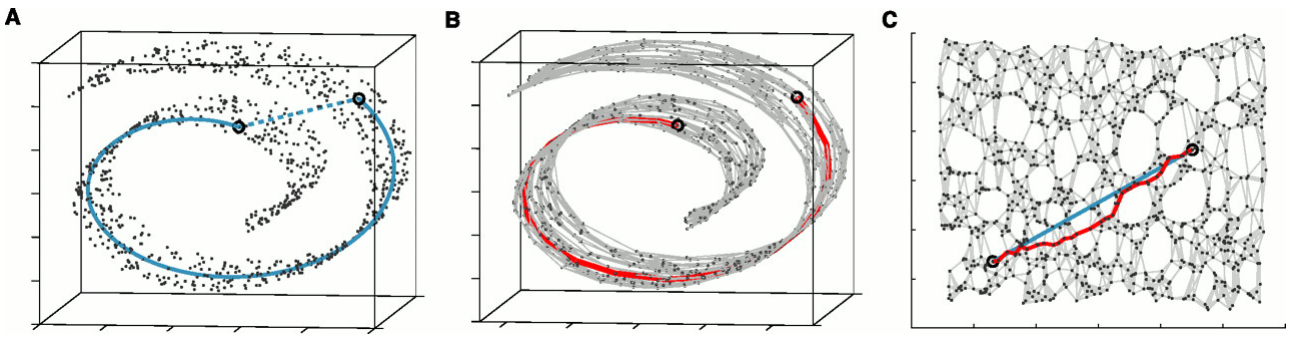

Figure 2.5: Steps of Isomap Algorithm(adopted from [6]).

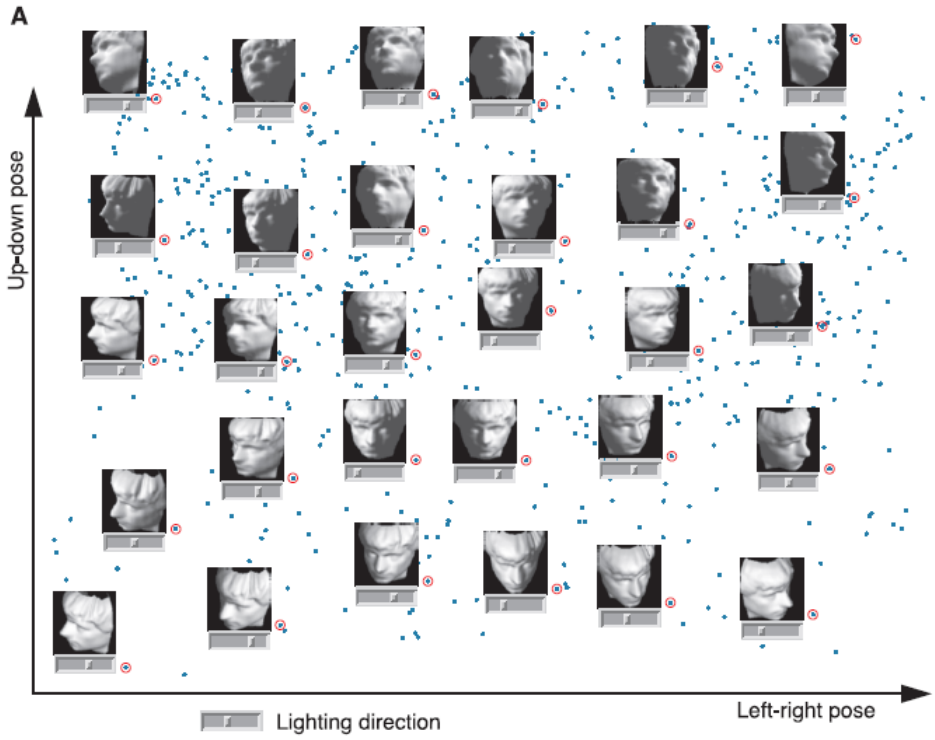

Figure 2.6: Isomap Result, showing the variation of light in left-right direction; and variation of up-down pose in up-down direction (adopted from [6]).

After the geodesic distances, matrix D_G , is calculated; MDS (See Section 2.1.3) is applied on the distances in order to reduce the dimension.

One drawback of the Isomap is that it does not provide a general mapping that can map a new test point without running the algorithm again. Another drawback is that the algorithm is sensitive to the neighborhood parameters.

2.2.2 Locally Linear Embedding(LLE)

The motto of locally linear embedding is: "Fit Locally, Think Globally" [7]. In other words, it assumes that local patches of the manifold can be approximated linearly by writing each data point as a linear combination of its neighbors. With this assumption, given points, $X = \{x_1, x_2, ..., x_N\}$ the method minimizes the reconstruction error

$$\epsilon(W) = \sum_i \left| x_i - \sum_j W_{ij} x_j \right|^2 (2.6)$$

where the weights W_{ij} summarize the contribution of the jth data point to the ith reconstruction. Function is minimized with least squares subject to $\sum_j W_{ij} = 1$ and $W_{ii} = 0$ for all i.

After the W_{ij}s are calculated, a linear mapping y_i of the point x_i is found by using the previously fixed weightings by minimizing the following function:

$$\epsilon(Y) = \sum_i \left| \bar{y_i} - \sum_j W_{ij} \bar{y_j} \right|^2 (2.7)$$

The three steps of LLE algorithm is shown in Fig.2.8 clearly. In step 2, the weightings are calculated and in step 3, projections are calculated.

As with the Isomap, LLE can also not find a general mapping to project a new high-dimensional test point and is sensitive to neighborhood parameter. As stated in [21], different neighborhood relations can be used in different linear patches of the manifold, but it is still open to research. In literature, a special LLE called Hessian LLE exists. This method is very similar to LLE but it computes embedding based on Hessians.

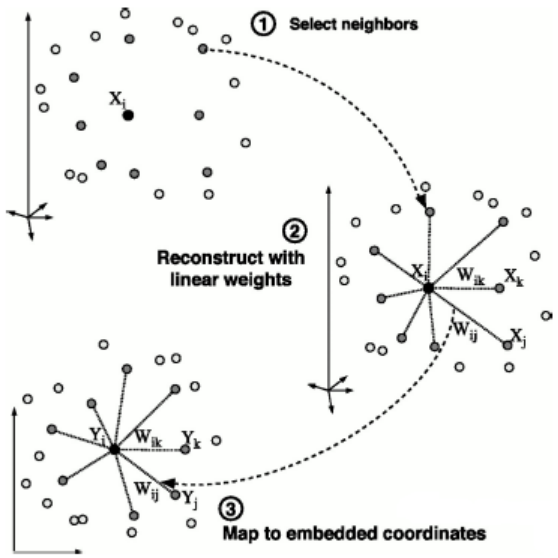

Figure 2.7: Steps of LLE Algorithm (taken from [7]).

2.2.3 Laplacian Eigenmaps

Laplacian Eigenmap[8] uses a similar idea to Isomap and LLE. Different from Isomap and LLE, this approach computes a low-dimensional projection of the data using the notion of a Laplacian of the graph. This embedding reflects the intrinsic geometric structure of the manifold. The algorithm is relatively insensitive to noise and outliers since it uses Laplacian-Beltrami operator [8]. It is an effective, geometrically motivated technique, which is used to solve a variety of vision problems such as segmentation, registration, tracking and object recognition. The technique was validated to be successful, particularly if the input has smooth appearance variation or smooth deformation[8].

Similar to Isomap and LLE, this approach incorporates the neighborhood information of the input to build a weighted graph. After building the graph, a low-D representation of the input that optimally preserves local neighborhood information, is computed by using the Laplacian of the graph. It is worth noting that, since the approach is geometrically motivated, the resulting mapping will be a discrete approximation of a continuous map from the high dimensional space to the low-D manifold.

The first step is to construct a graph G with representative k nodes for each x_i and edges between the nodes x_i and x_j , if the nodes are close enough. The relationship of being close can

be defined as an ϵ neighborhood $||x_i - x_j|| < \epsilon$, where $||.||$ denotes the Euclidean norm. The disadvantage of this choice is the parameter setting. Another option is using n nearest neighbors, where one can put an edge between the nodes x_i and x_j if j is one of the n nearest neighbors of i.

Another important issue is defining a similarity measure for the nodes x_i and x_j. Most commonly used similarity measures, such as Sum of Squared Distances (SSD), Sum of Absolute Difference (SAD) or Normalized Cross Correlation (NCC) can be used.

It is assumed that the graph G, constructed in the previous step, is connected. The second step is to weight the edges in the graph by appropriate weights. The weight function is inspired from the heat kernel given by

$$W_{ij} = exp^{-||x_i - x_j||^2/2\sigma^2} \tag{2.8}$$

where σ^2 is the variance. $W = [W_{ij}]; ij \in [1, .., k]$, forms the weight matrix. In Fig. 2.9 the results for different values of σ(also called t) and N, number of nearest neighbors, can be seen.

Let $y = (y_1, y_2, .., y_k)^T$ be the desired mapping. A reasonable criterion for choosing a good map is to minimize the following objective function:

$$\sum_{ij} (y_i - y_j)^2 W_{ij}, \tag{2.9}$$

under appropriate constraints. The objective function with our choice of weights W_{ij} incurs a heavy penalty if neighboring points x_i and x_j are mapped far apart. Therefore, minimizing it is an attempt to ensure that if x_i and x_j are close, then y_i and y_j are close as well. Minimizing and manipulating the term in Eq.2.9, a generalized eigenvector problem is obtained as follows:

$$Lf = \lambda Df, \tag{2.10}$$

where D is a diagonal weight matrix, constructed by summing up the columns of W, $D_{ii} = \sum_j W_{ji}$. Here, Laplacian matrix L is calculated as $L = D - W$. Finally the eigenvectors corresponding to the smallest eigenvalues (excluding zero) of the Laplacian matrix gives the desired mapping. Further justification and details on the Laplacian Eigenmap method can be seen in [8].

(a)3D Swiss roll

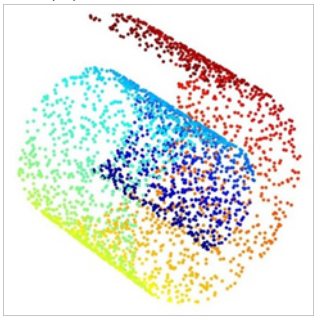

(b)Laplacian Eigenmap with different t and N

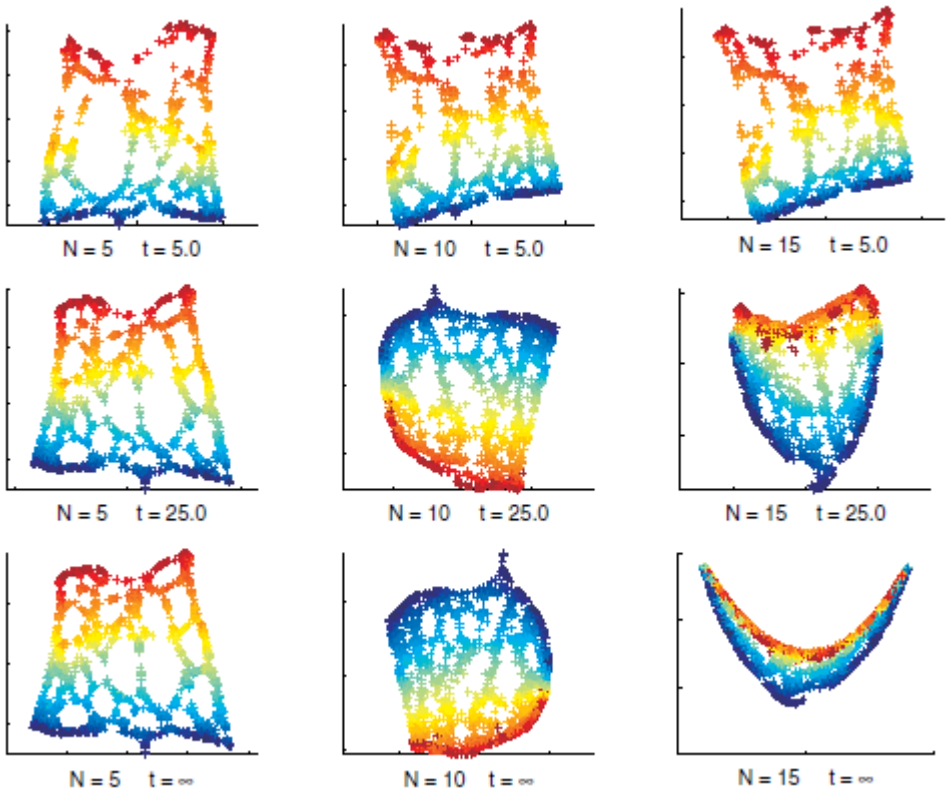

Figure 2.8: Parameters for Laplacian Eigenmap(taken from [8]).

This method is very simple and efficient since it solves only one sparse eigenvalue problem, thus is appropriate for large data sets.

In this chapter we presented nonlinear dimensionality reduction techniques(NLDR), Isomap, LLE and Laplacian Eigenmaps, which are also known as manifold learning techniques. They aim to find the best global mapping for high-D data, that preserves the local distances, assuming that high-D data live on a nonlinear manifold. All of these methods have common steps such as, finding k-nearest neighbors; estimating local properties of manifold by looking at the neighbors and finding a global embedding that preserves the properties of manifold. In Chapter 3, we make use of manifold learning concept for our gating problem.

Chapter 3

Manifold Learning for Image-based Gating

In Section 1.3.2 the previous solutions proposed for gating problem was introduced. In all the previous methods, even if different approaches were used, the overall objective is to be able to construct a 1D signal similar to R-waves by using the information(features) that is embedded in the images in order to do gating.

All of the previous methods require preprocessing or postprocessing in order to extract valuable information from the images. In [13] and [20], the dissimilarity matrix is filtered as a preprocessing step, in [11], a region of interest is extracted before the signal is calculated and in [10], the signal is calculated in polar domain, which requires conversion from display domain. Since the IVUS images in polar domain are not available most of the time, as the scan-converted display IVUS images are typically in use, it can also be counted as a preprocessing step. Similarly all the methods employ a bandpass filter to the extracted signals for noise reduction.

All of the previous methods focus on certain signals that is based on certain properties of images such as: average intensity, absolute intensity difference or motion blur signal. However there may be additional information buried in one image, thus focusing on only one feature may prevent us from extracting a better signal. Therefore, to make use of all the information embedded in the images we propose projecting our high-dimensional data, to a low-dimensional manifold, which can be achieved with manifold learning techniques that was explained in details in Chapter 2.

Manifold learning is an effective, geometrically motivated, nonlinear dimensionality reduction technique, which is used to solve a variety of vision problems such as segmentation, registration, tracking and object recognition. Detailed information can be found in Chapter 2, Section 2.2. The technique was validated to be successful, particularly if the input has smooth appearance

variation or smooth deformation[8]. As explained in Chapter 1, Section 1.2, cardiac cycle's first effect, slowly varying longitudinal movement of the catheter, results in a smooth appearance variation. Furthermore, the slight vessel morphology change during the cycle results in a smooth deformation in the input images. Due to the fact that the cardiac cycle is almost periodic and the frames that belong to the same cardiac cycle look more similar than those that were acquired during another cardiac cycle, a neighborhood relationship between IVUS images is present. Manifold learning methods also utilize the spatial/neighborhood information in the pullback and that makes the method suitable for our problem.

In this thesis, our goal is to develop an algorithm that is efficient, does not require preprocessing, preserves locality and extracts a better 1D signal to differentiate cardiac cycles. We propose directly projecting our high dimensional data, to a low-dimensional manifold and thus treating each image frame as a low-D signal in the low-D manifold; instead of extracting features from each frame.

One of the questions that may arise is why we choose manifold learning method as our dimensionality reduction technique. In order to answer that, the most commonly used linear dimensionality reduction techniques such as Principal Component Analysis(PCA) and Multi-dimensional scaling(MDS) are efficient and simple, however are not able to detect nonlinear structures that exist almost in all real datasets. The human cardiac system is nonstationary and dynamic; hence, linear analyses may not account for all aspects of cardiac performance[25],[26]. In addition, in the lesion areas where the cross-sectional view of the vessel can change faster, using global distance metrics would fail because the lesion areas would be detected as outliers. However manifold learning preserves locality, which makes it much less sensitive to noise and outliers.

Isomap [6], local linear embedding(LLE) [7], and Laplacian eigenmaps [8] are three popular different techniques for manifold learning. In this work we use Laplacian eigenmaps technique (see Section 2.2.3 for a mathematical background). Another question that may arise is why we choose Laplacian Eigenmaps among the three popular manifold learning algorithms.

The general properties of our data can be summarized as follows:

- IVUS pullback is high-dimensional(usually around 500x500x3000).
- There are small variations between the consecutive frames. Hence, the data does not consist of very densely sampled clusters.

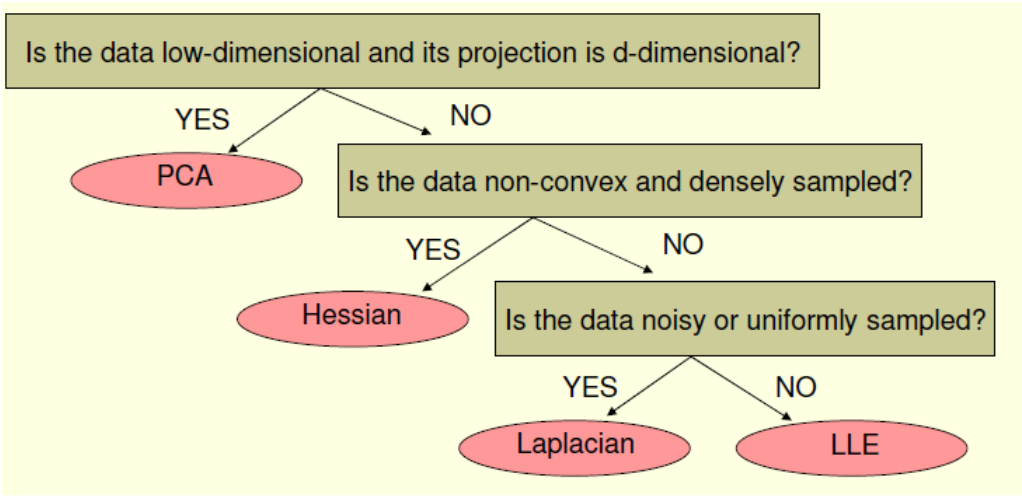

Figure 3.1: Decision tree for manifold learning techniques(taken from [9]).

- IVUS data is considered to be noisy, due to the lesion areas and ultrasound's speckled appearance.
- Data is almost uniformly sampled using a constant speed motor.

Our data is not low-dimensional but its projection is d-dimensional, where d denotes 2 or 3. Our data is assumed to cluster in a non-convex domain, where non-convex means that the line segment connecting two points in the domain does not necessarily lie within the domain, but our data is not densely sampled. Finally due to the fact that our data is noisy and uniformly sampled, following the decision tree in Fig. 3.1 we are led to Laplacian Eigenmaps method.

Table 3.1 presents a comparison among the NLDR techniques. As it is shown here, the Laplacian Eigenmap method does not handle non-uniform sampling and clusters. However, this does not affect our algorithm since our data properties are completely in line with what the Laplacian Eigenmaps method expects.

In addition, another advantage to use Laplacian Eigenmaps method is its efficiency and simplicity since it solves only one sparse eigenvalue problem.

In order to illustrate the idea of manifold learning on our problem, a desired mapping for 9 sequential cardiac cycles is given in Fig. 3.2. In Fig. 3.2, the low-D manifold gives a nice intuition of the clusters that belongs to the same cardiac cycle. Each cluster is shown with a different color and assumed to represent a different cardiac cycle. Different cardiac cycles seem to be well-seperated from each other.

	MDS	PCA	ISOMAP	LLE	Hessian	Laplacian	Diffusion Map	KNN Diffusion
Speed	Very slow	Extremely fast	Extremely slow	Fast	Slow	Fast	Fast	Fast
Infers geometry?	NO	NO	YES	YES	YES	YES	MAYBE	MAYBE
Handles non-convex?	NO	NO	NO	MAYBE	YES	MAYBE	MAYBE	MAYBE
Handles non-uniform sampling?	YES	YES	YES	YES	MAYBE	NO	YES	YES
Handles curvature?	NO	NO	YES	MAYBE	YES	YES	YES	YES
Handles corners?	NO	NO	YES	YES	NO	YES	YES	YES
Clusters?	YES	YES	YES	YES	NO	NO	YES	YES
Handles noise?	YES	YES	MAYBE	NO	YES	YES	YES	YES
Handles sparsity?	YES	YES	YES	YES	NO *may crash*	YES	NO	NO
Sensitive to parameters?	NO	NO	YES	YES	YES	YES	VERY	VERY

Table 3.1: NLDR Comparison(taken from [9]).

As a reminder for Laplacian Eigenmaps, the neighborhood information of the input is incorporated to build a weighted neighborhood graph $G =< X, E >$, where the nodes correspond to N points: $X = \{x_1, x_2, ..., x_N\}$ and edges E correspond to the weights between each pair of nodes. In our specific application, each vessel cross-section at a certain cardiac phase is represented as a two-dimensional, 500x500 image, that corresponds to nodes x_i of our weighted graph G. Thus, we can say that each cross-section acquired at some cardiac phase is a point with 250,000-dimensions. As cross-section images of vessels are taken by pulling the catheter back with a slow speed; the sequence of images we capture follows a trajectory in the 250,000-dimensional space which is not linear. These trajectories define a manifold in the 250,000-dimensional space, which we want to model. After building the graph, a low-D representation of the input that optimally preserves local neighborhood information, is computed by using the Laplacian of the graph. It is worth noting that, since the approach is geometrically motivated, the resulting mapping will be a discrete approximation of a continuous map from the high dimensional space to the low-D manifold.

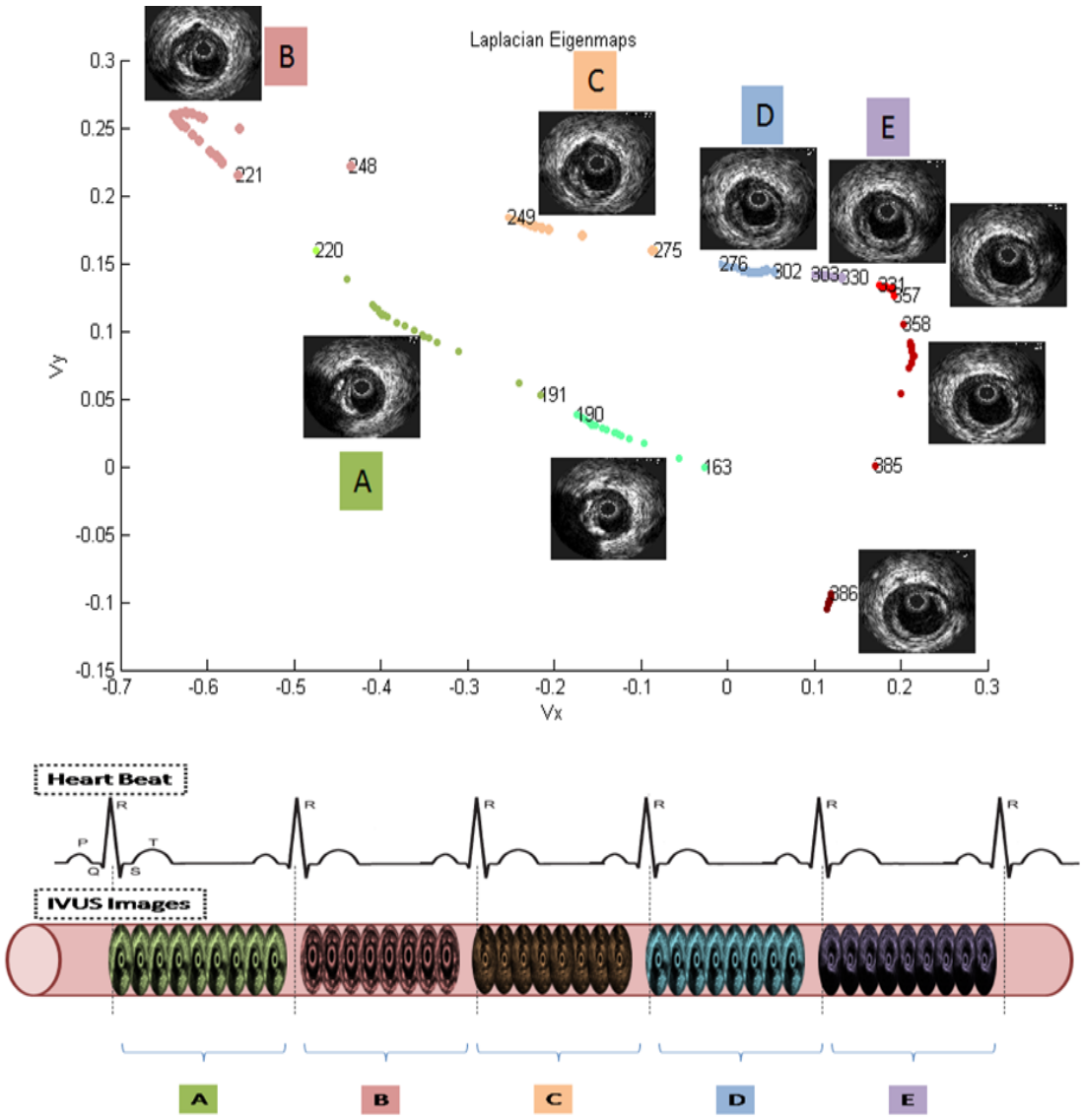

Figure 3.2: An illustration of Manifold idea. Each frame is shown with a dot on the calculated low-D manifold(here m=2), where A,B,C,D,E are the clusters of frames that belong to different cardiac cycles.

3.1 Parameters

Laplacian Eigenmaps require three different parameters as was introduced in Section 2.2.3. These parameters are: neighborhood definition; σ value in the heat kernel equation; and distance definition between the images. Selection of these parameters for the given problem in this thesis will be explained in the following subsections.

3.1.1 Neighborhood

The neighborhood information is used during the weighted graph building step. The relationship of being close can be defined as an ϵ neighborhood $||x_i - x_j|| < \epsilon$, where $||.||$ denotes the Euclidean norm. If this option is preferred than the edge weight W_{ij} between two ϵ neighbor IVUS images x_i and x_j are assigned to 1 in order to connect them; otherwise the edge value is assigned to 0. Another option is using n nearest neighbors, where one can put an edge between the nodes x_i and x_j if j is one of the n nearest neighbors of i. When this option is used, the edges between x_i, x_{i+1}, ..., x_{i+n} are assigned to 1 and the the edges between x_i, x_{i+n+1}, ... , x_k are assigned to 0.

This step can be seen as a preliminary step for building weighted neighborhood graph. In this step only the connections between the nodes are determined by putting the values 0 and 1. The graph that is built in this step can be used directly for a simple-minded approach, however for advanced results, weighting the edges between 0 and 1 with a heat kernel weight function is employed.

3.1.2 Heat Kernel Parameter, σ

σ^2 is defined as the variance that is used in the heat kernel weight function:

$$W_{ij} = exp^{-d(x_i,x_j)/2\sigma^2} \tag{3.1}$$

where $d(x_i, x_j)$ is the distance between x_i and x_j and $W = [W_{ij}]; ij \in [1, .., k]$, forms the edge weight matrix. $W_{ij} = 0$, if the data points x_i and x_j are not connected according to the chosen neighborhood relationship. W_{ij} is close to 1, if x_i and x_j is close enough(similar enough) according to the value of $d(x_i, x_j)$.

In this step, the neighborhood graph that was built in the previous step is weighted only for the connected nodes.

3.1.3 Similarity Measure

Similarity measure is used to define the distances $d(x_i, x_j)$ between image pairs, which appears in Eq. 3.1. Squared Euclidean distances is the most commonly used measure for calculating

distances. In this work, we propose a novel similarity measure "Weighted Speckle Distance" specially designed for ultrasound images to get more meaningful distances.

Sum of Squared Distances(SSD)

Sum of squared distances is defined as

$$d(X,Y) = ||X - Y||^2 \tag{3.2}$$

where X,Y are matrices with same dimension and $||.||$ denotes the Euclidean norm.

Weighted Speckle Distance(WSD)

It can be observed that size of speckle in ultrasound images increases as the distance between the probe and the tissue to be imaged increases. This can be interpreted as the reliability of information in IVUS images decrease from near field towards the far field, i.e., as we go away from the catheter. In the presence of this information, we design a new similarity measure, where we weight the similarities of the pixels according to their distances to the catheter center, which is also the image center. In other words, the similarity of a pixel that is close to center contributes more to the total distance between the images. In order to do that, we use a logarithmic sigmoid function defined as

$$dw(z) = 1 - \frac{1}{1 + \exp(-z)} \tag{3.3}$$

In this equation z is the shifted radial distance from the catheter, starting from -$\sqrt{m}/40$ to $+\sqrt{m}/40$, where m is the maximum distance from the catheter. The resulting function can be seen in Fig. 3.3.

The filter, DW, is designed by shifting and scaling the transfer function to fit the image size. In Fig. 3.4 a) the filter in polar domain and in b) the filter in display domain is shown.

The IVUS images are weighted with the filter shown in Fig. 3.4 and finally SSD is used to calculate the distances as:

$$d(X,Y) = ||DW * X - DW * Y||^2 \tag{3.4}$$

where * denotes multiplication.

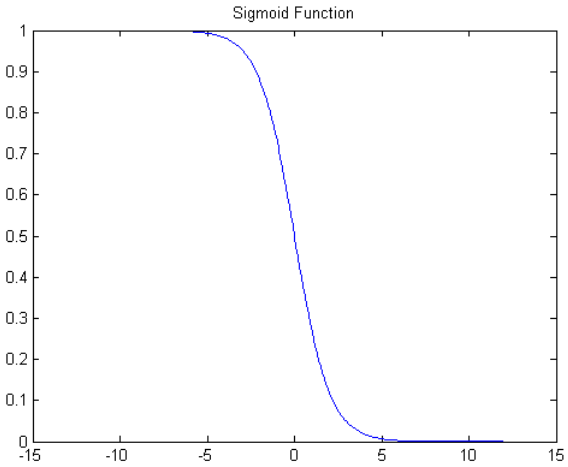

Figure 3.3: Transfer function.

a) Sigmoid function as an image in polar domain

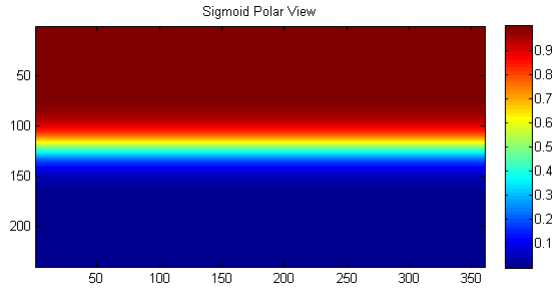

b) Sigmoid function as an image in display domain

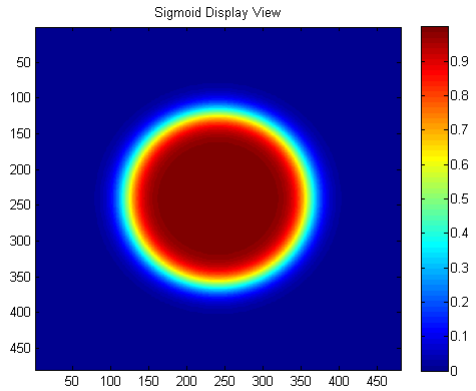

Figure 3.4: Sigmoid Function as a Filter.

Projection Dimension

An important issue is the choice of the dimension of the $\mathcal{M}$, denoted by m. We need one dimension to account for the smooth appearance variation caused by the first vessel morphology change, and another dimension to account for the smooth deformation caused by the catheter motion. Thereby, we set $m \geq 2$, and we heuristically choose $m = 3$. In another word we choose to represent each image frame with a 3D vector which gave satisfactory performance as will be demonstrated in the experiments.

After the distances and parameters are defined as described above, the weight matrix W is constructed, and its Laplacian matrix is formed. A generalized SVD analysis on the Laplacian matrix follows, which produces the 3D projection vectors V_i for each IVUS image x_i.

3.2 1D Signal Extraction

At this point in our method, we projected each IVUS image x_i to a 3D vector V_i. Recall that our goal is to obtain a 1D signal similar to an R-wave (not exactly corresponding to systole, diastole and so on phases), but to be able to extract a signal that differentiates between different cardiac cycles, and allows us to sample from a similar point in the cycle for all cycles. For this purpose, we construct a distance signal , $d = ||V_{i+1} - V_i||$, where $||.||$ denotes the Euclidean norm and V_i denotes the 3D projection vector of the image x_i, where $i = \{1, 2, ..., N\}$. In Fig. 3.5, a sample of the constructed d function for 400 IVUS frames is shown for illustration, where green boxes indicate the local maxima points in d function.

3.3 Parameter Selection

In order to choose the best parameters, we used different in-vitro datasets with ground truths and different values for all parameters and analyzed the differences between our results and the ground truth.

3.3.1 In-Vitro Data

In [10], the authors introduce a mechanical device that consists of a rotating wheel which is connected to a transversal arm generating horizontal swinging oscillations. The oscillation speed

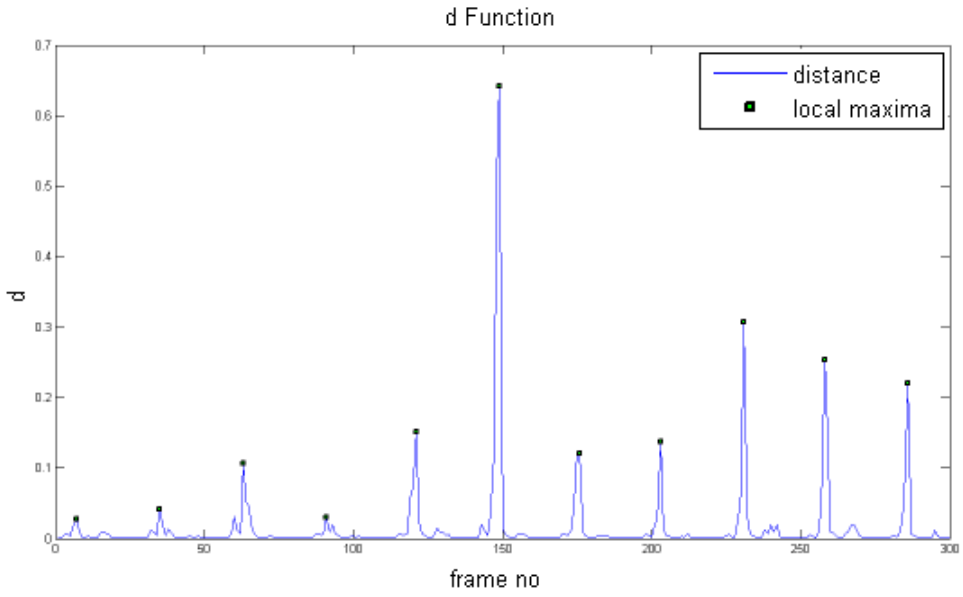

Figure 3.5: Normalized Distance Function.

can be controlled by the user by changing the power supply Voltage.

We acknowledge the help of authors of [10] who shared with us their data set, which consisted of 20 different pullbacks that were generated with the mentioned set-up specifically constructed for creating validation data for IVUS gating algorithms.

We applied our algorithm on 20 different pullbacks acquired from 3 different post-mortem arteries with frequencies $F = \{50, 60, 70, 80\}$ BPM(Beats Per Minute), which are inversely related to the oscillation periods of the catheter.

In order to interpret our results, we calculated $Y(jw)$ Fourier transform of our signal $d(t)$. In Fig. 3.6, an example for the amplitude spectrum of $Y(jw)$ is shown. The harmonics of the signal can easily be noticed as peaks. To validate our method, we statistically analyzed the frequencies of the first four harmonics of $Y(jw)$ by employing coefficient of variation (CV), defined as:

$$CV = \frac{\sigma}{\mu} \tag{3.5}$$

where σ is the standard deviation of the first four harmonics and the μ is the ground truth frequency for the pullback that is being analyzed[1]. The coefficient of variation is useful because

[1]We note that in the usual definition of CV, the standard deviation is normalized by the mean of the data samples. Here, we used the true value rather than the sample mean to analyze the dispersion of the estimated harmonic frequencies around the true frequency.

the standard deviation of data must always be understood in the context of the mean of the data. Here we could use CV, since the oscillation frequencies are always positive, therefore the mean is always larger than zero. In-vitro data analysis aided us in parameter selection of our method, as the true oscillation frequency, which emulates heart beats, is known. This analysis is given next.

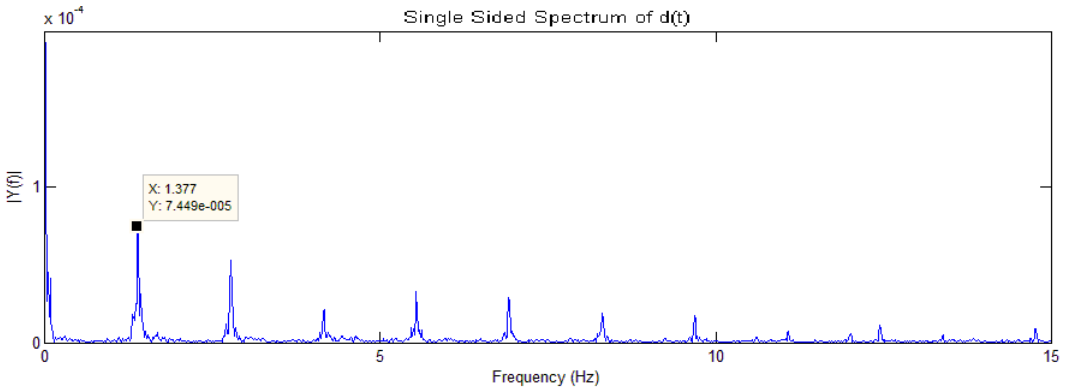

Figure 3.6: amplitude spectrum of $d(t)$.

3.3.2 Neighborhood Selection

We tested our method with ϵ neighborhood and $n = \{1, 10, 15, 20, 30, 40, 60\}$. The longer the heart beat is, the less frames are acquired during one heart beat, since the frames per second, fps, stays constant. In other words, greater the beats per minute, less neighbors we shall need for the algorithm.

We calculated CV for each dataset and analyzed each frequency category separately. The smaller CV indicates less dispersion.

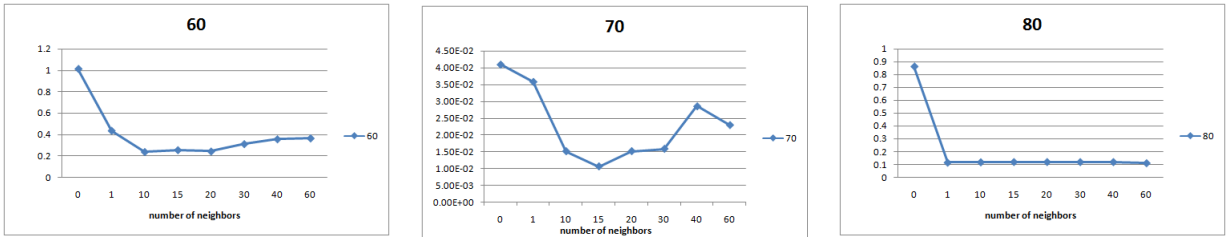

(a) (b) (c)

Figure 3.7: (a)CV Performance for 60 BPM (b)CV Performance for 70 BPM (c) CV Performance for 80 BPM.

In Fig. 3.7, the coefficient of variation values for different parameter values are shown. Please note that zero neighbor represents ϵ neighborhood. When the beats per minute is 60, the values $n = 10, 15, 20$ perform similarly and good, however as n is increased to 30 the performance starts getting worse. As we have predicted earlier 70 BPM should need less neighbors. As can be seen from the Fig. 3.7 b), the best performance is when $n = 15$, and the performance decreases when n is increased to 20. Similarly with 80 BPM , the critical value is $n = 1$.

To conclude, the results we get in this experiment support our assumption and also shows the importance of the neighborhood parameter. Since the average heart rate for human beings is around 60-70 BPM, we choose $n = 15$ as our neighborhood parameter in our in-vivo experiments.

3.3.3 σ Selection

In Fig. 3.8, the CV values are shown for $\sigma = \{10, 50, 100, 150\}$. The best performance occurs when $\sigma = 50$, so we choose heat kernel parameter in the weight function defined in Eq. 3.1, $\sigma = 50$. However the differences between the CV values of different σ values are not so distinguished, thus we can conclude that it is not a very critical parameter for our dataset.

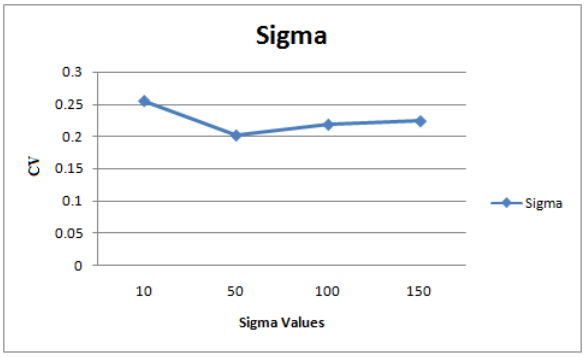

Figure 3.8: Sigma Choice.

3.3.4 Similarity Measure Selection

Our algorithm is tested with SSD (Sum of Square Distances)given in Eq. 3.2 and WSD(Weighted Speckle Distance) given in Eq. 3.4. In Fig. 3.9, it can be seen that the CV value of WSD is lower than the CV value of SSD. We comment that WSD measure acts superior to SSD. Also, in Fig. 3.10, the spectrum results of $d(t)$ of the same pullback using SSD and WSD is shown. It can be noticed that sharper peaks of the harmonics can be seen in the spectrum of WSD. This

shows that, WSD helps us to get rid of the noise and focus more on meaningful data, which correspond to peaks of the harmonics in this case.

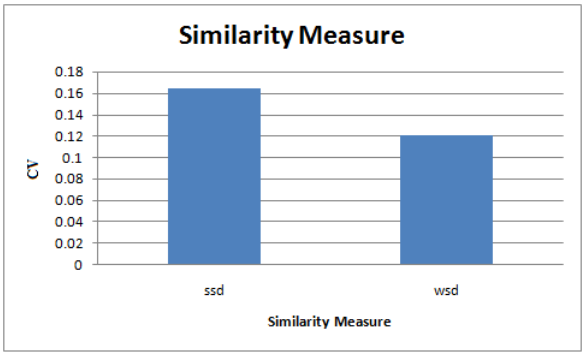

Figure 3.9: Similarity Measure Choice.

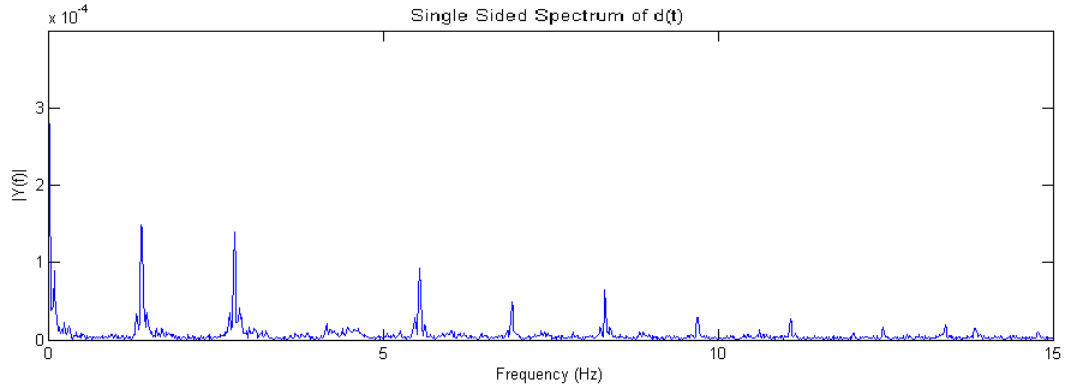

(a)

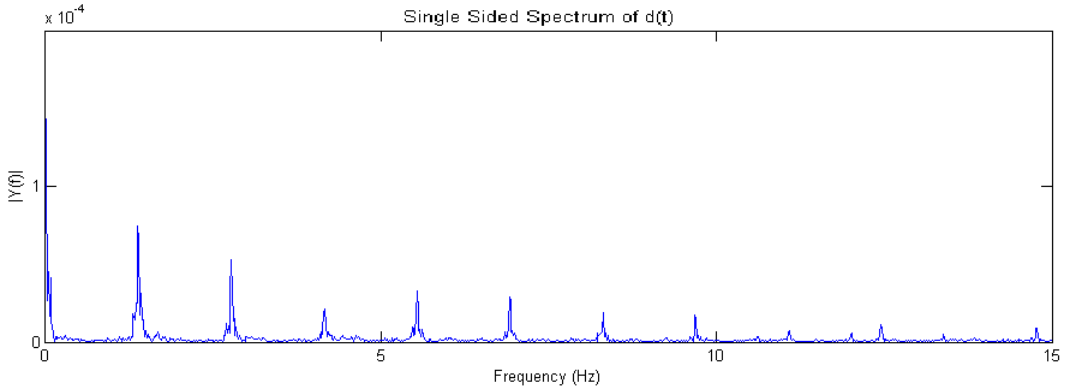

(b)

Figure 3.10: Spectrum Comparison a)Amplitude Spectrum of $d(t)$ using SSD b)Amplitude Spectrum of $d(t)$ using WSD.

3.4 Gating

In our method, we used n_{cycle} to represent roughly the number of frames per cardiac cycle. n_{cycle} is defined as $f_{Rate}/1.2Hz$, where 1.2 Hz is the average heart beat rate of human species[14] and f_{Rate} is the frame rate of the pullback. Similarly $min_{cluster}$ is used to represent the minimum number of frames in a cardiac cycle. $min_{cluster}$ can be equated to $f_{Rate}/(1.2Hz + 2\sigma)$, where σ is the variance of the heart beat rate and n_{cycle} is the average number of frames per cardiac cycle. Similarly, $max_{cluster}$ can be equated to $f_{Rate}/(1.2Hz - 2\sigma)$.

The final part, choosing the stable frames, so called gating, is performed on the constructed 1D signal $d(t)$ in Section 3.2. In our gating algorithm, the distance signal is treated like a composition of small constant size patches of signals.

The frame numbers where global maximum occurs, is found in each patch, then starting from each maximum point, local maxima points that lie between the interval $(currentInd + min_{cluster}) - (currentInd + max_{cluster})$ are added to the gated frame list and last chosen frame is updated accordingly. Algorithm continues till no interval can be found. This whole process presented in pseudo code 3.4. Finally, the gated frames found for each patch are merged.

1: $startInd \leftarrow maxval$
2: $currentInd \leftarrow startInd$
3: $c \leftarrow 1$
4: $k \leftarrow 0$
5: **while** c **do**
6: $\quad minInd \leftarrow currentInd + min_{cluster}$
7: $\quad maxInd \leftarrow currentInd + max_{cluster}$
8: $\quad positions \leftarrow minInd : maxInd$
9: $\quad n \leftarrow max_{cluster} - min_{cluster}$
10: $\quad$ **for** $i = 1$ **to** n **do**
11: $\quad\quad$ **if** $positions(i) \in localMaxPointsSet$ **then**
12: $\quad\quad\quad currentInd \leftarrow positions(i)$
13: $\quad\quad\quad gatedInd(k) \leftarrow currentInd$
14: $\quad\quad\quad c \leftarrow 1$
15: $\quad\quad\quad k \leftarrow k + 1$

16: **end loop**

17: **end if**

18: $c \leftarrow 0$

19: $i \leftarrow i + 1$

20: **end for**

end while

A sample result is shown in Fig. 3.11 for demonstration. Longitudinal IVUS views shown in Fig. 3.11 demonstrate similar qualitative outcome for our manifold-learning based IVUS gating method, and the ECG-gated method.

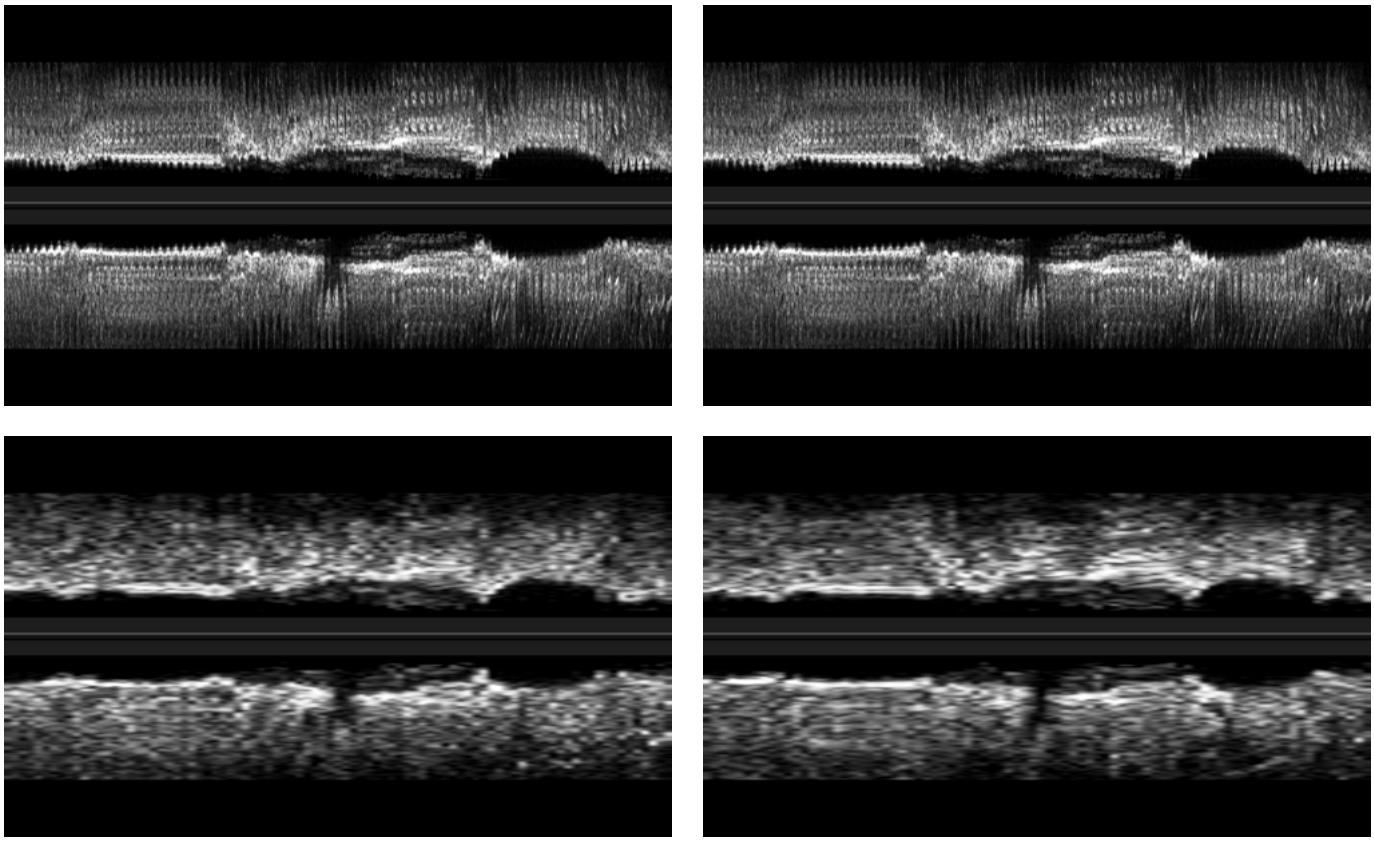

Figure 3.11: *First row:* Nongated pullback. *Second Row; Left:* Image-based gated pullback. *Right:* Ecg gated pullback.

Chapter 4

Experimental Results and Discussion

4.1 In-Vivo Data

We applied our automatic image-based gating algorithm on 12 different patients from two different hospitals and 25 different pullbacks. All the pullbacks were acquired in-vivo in the coronary arteries of the patients of our clinical partners with 20 MHz IVUS catheter. The frame rate was 30 Hz and the motorized pullback speed was 0.5 mm/s.

4.2 Validation

In order to validate our method we compared the results of our algorithm with the results of ECG Gating. As stated in Section 1.1, we claim that image-based gating preserves the lumen volume, plaque configuration and the length of the artery. For that reason our validation is based on measuring the preservation of these values.

In this section we mostly compare our results with ground truth data. For that reason, we used a statistical analysis: Bland-Altman plot, that shows/measures the agreement between two methods. The construction of the plot is as follows: Given n samples and $n + n = 2n$ measurements, one from the method to be compared and one from the ground truth(gold standard); the mean of the two measurements are assigned as x-axis, while the difference between the two values as the y-coordinate. One can also compute the limits of agreement. In our experiments, we specified it as bias ± 1.96 STD, which corresponds to 95% confidence level. An example Bland-Altman plot can be seen in Fig. 4.2.

4.2.1 Lumen Volume Comparisons

As stated in Section 1.1, the accurate measurements of lumen is crucial for coronary artery diseases' diagnostics. For that reason, we compared the lumen areas calculated from our gated pullbacks and ecg gated pullbacks. The lumen areas were drawn by the expert cardiologists in our team. To approximate lumen volume, we compared the lumen areas in the longitudinal views of the vessel from 4 different angles for each pullback. In Fig 4.2.1, an illustration of vessel longitudinal cuts at different angles is given. Difference(LAD) error in Table 4.1 is calculated as the ratio of the absolute difference of the areas found by the two methods, with the ecg-gated pullback area used as the ground truth: $LAD_{error} = |LA_{ecg} - LA_{alg}|/LA_{ecg}$, where LA_{ecg} is the lumen area in the ecg gated pullback and LA_{alg} in the image based gated pullback. An LAD error rate of 0.08 ± 0.04 is obtained. In addition, a Bland-Altmann analysis on the lumen areas in Fig. 4.2, revealed that more than 95% of the measurements were in agreement between the two methods.

4.2.2 Phase Analysis

One interesting analysis for an image-based gating algorithm is to examine the cardiac phases from which the gating frames are selected and investigate if there is consensus for the selected cardiac phases in all cardiac cycles. We note here that, for an image-based algorithm, as there is no ECG sensor or device information is present, and solely image features are used for gating, only a reasonable agreement among cardiac cycles over a common selected phase is expected. For that purpose, we analyze the phases from which our algorithm picks the stable frames as follows: the interval between two subsequent frames that are picked by ECG, is divided into ten bins where each bin represents a different cardiac phase. In Table 4.2, the columns represent the bins. As an example, let us consider that the cardiac cycle is 100ms, then the column, $10\% - 20\%$, represents the time interval 10ms-20ms. The columns in Table 4.2, represents the percentile of the gated frames chosen from that specific cardiac phase, which is calculated as $(framesChosenInPhase/totalFramesChosen)$x100. In this analysis: if the value for $10\%-20\%$ is 30, it means that the 30% of the frames chosen by our algorithm are chosen between the first 10ms-20ms of the RR cycle.

According to Table 4.2, average of approximately 70% of our stable frames were picked between 30% and 60% of the cardiac phase.

pt_{id}	pb_{id}	LC 10°	LC 55°	LC 100°	LC 150°	$MeanError$	std
1	1	0.24	0.09	0.01	0.02	0.09	0.11
1	2	0.24	0.08	0.02	0.04	0.09	0.10
2	1	0.05	0.04	0.00	0.00	0.02	0.03
2	2	0.08	0.09	0.04	0.04	0.06	0.03
2	3	0.06	0.06	0.09	0.05	0.07	0.02
2	4	0.02	0.05	0.02	0.01	0.02	0.02
2	5	0.09	0.08	0.02	0.02	0.05	0.04
3	1	0.19	0.03	0.02	0.02	0.06	0.08
3	2	0.05	0.03	0.14	0.18	0.10	0.07
4	1	0.19	0.00	0.10	0.13	0.11	0.08
5	1	0.31	0.13	0.15	0.10	0.17	0.09
6	1	0.23	0.01	0.02	0.00	0.07	0.11
6	2	0.16	0.06	0.12	0.10	0.11	0.04
6	3	0.20	0.01	0.06	0.04	0.08	0.08
7	1	0.16	0.05	0.10	0.07	0.10	0.05
7	2	0.05	0.04	0.07	0.13	0.07	0.04
8	1	0.18	0.02	0.02	0.06	0.07	0.08
8	2	0.02	0.05	0.10	0.01	0.04	0.04
9	1	0.37	0.13	0.05	0.22	0.19	0.14
9	2	0.30	0.01	0.16	0.05	0.13	0.13
10	1	0.05	0.00	0.01	0.11	0.04	0.05
10	2	0.05	0.01	0.04	0.10	0.05	0.04

Table 4.1: Lumen Area Differences Error Analysis, where pt_{id} is the patient id, pb_{id} is the pullback id, angle is the viewing angle for constructing a longitudinal cut and the values under angles represent the lumen area difference error.

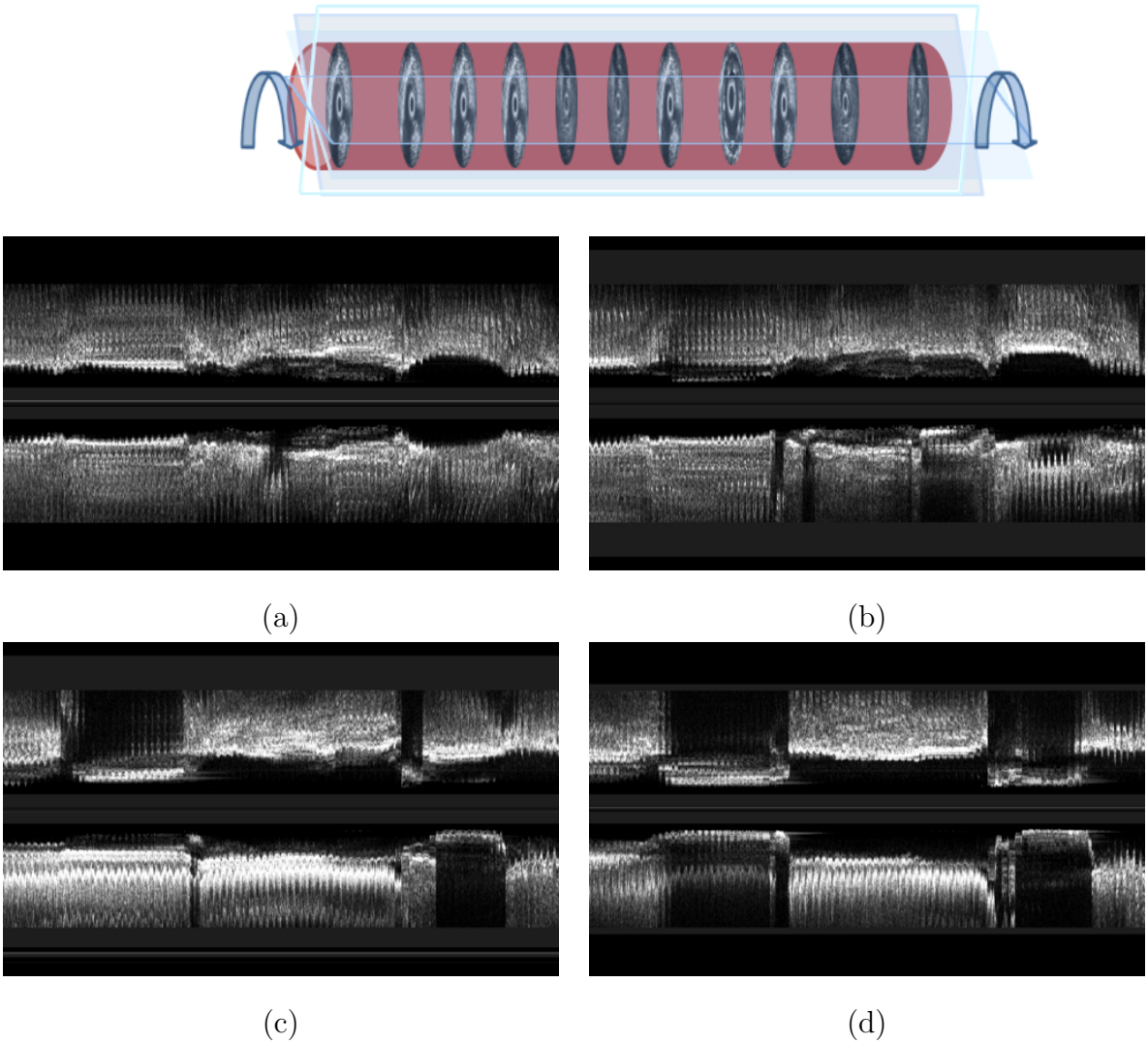

(a) (b)

(c) (d)

Figure 4.1: Top:An illustration of longitudinal cuts(LC) at different angles (a) LC from 10° (b) LC from 50° (c) LC from 130° (d) LC from 150°.

4.2.3 Frame Count Difference

In order to validate our results, we compared the number of gated frames obtained by our algorithm and by ECG gating algorithm. In Table 4.3, the number of gated frames from the two methods show agreement. In Fig. 4.3, a plot for the Bland-Altmann analysis based on the number of gated frames calculated by both methods, however with a bias(underestimation) in the mean, is given. This analysis showed that more than 95% of the measurements were in agreement between the two methods. To account for the different vessel lengths among our dataset, we considered the normalized counts, computed as #gated / #total. A normalized frame count difference error rate of 0.0789 ± 0.05 is obtained.

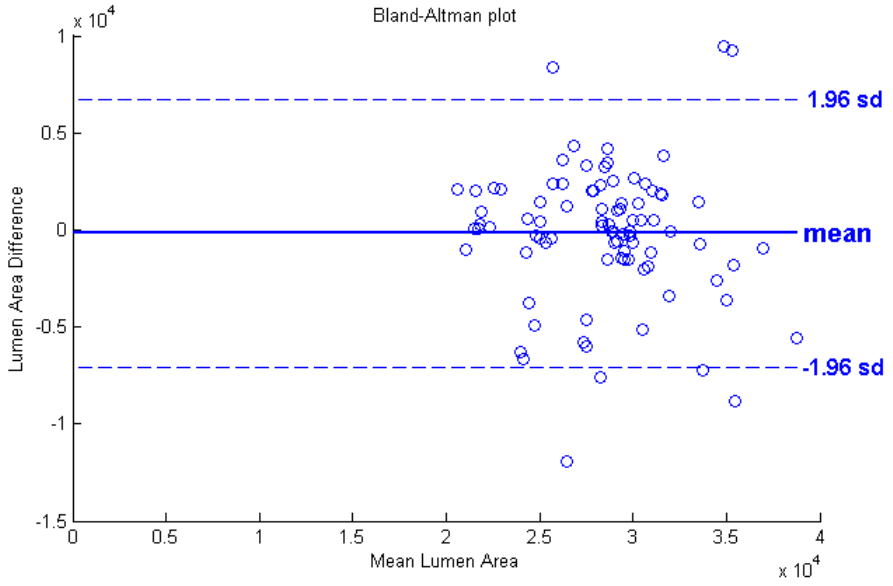

Figure 4.2: Bland-Altmann Analysis of Lumen Areas drawn by the medical experts on ecg gated pullback and image-based gated pullback: 185 ± 59.27 pix; $0.12\% \pm 0.03\%$.

0% – 10%	10% – 20%	20% – 30%	30% – 40%	40% – 50%	50% – 60%	60% – 70%	70% – 80%	80% – 90%	90% – 100%
2,38	1,19	1,9	35,24	30,48	5,9	6,9	5,71	4,52	4,76
1,14	3,45	2,68	38,31	32,49	12,68	2,68	2,04	2,23	2,04
3,53	1,18	1,18	33,24	31,18	6,47	6,76	7,06	5,88	3,53
3,9	3,9	3,9	31,88	29,68	5,58	5,39	4,09	7,79	3,9
6,25	3,75	3,75	41,25	41,25	8,75	8,75	2,5	2,5	6,25
3,85	0	3,85	35,77	28,08	9,23	7,69	7,69	0	3,85
6,41	2,56	2,56	39,49	31,79	6,67	5,26	2,69	1,28	1,28
9,52	3,57	2,38	34,76	24,29	13,1	1,71	4,76	4,76	2,14
8,64	1,23	3,7	33,46	28,52	1,11	4,88	3,64	7,41	7,41
3,85	5,13	17,95	27,95	15,38	11,54	4,1	6,41	7,69	0
1,37	0	5,48	35,55	25,55	6,44	8,7	5,96	4,11	6,85
6,25	5	15	28,75	20	11,25	2,5	5	5	1,25
2,44	0	8,54	38,05	31,95	2,2	2,2	7,32	2,44	4,88
4,82	8,43	13,25	14,46	14,46	14,46	10,84	4,82	4,82	1,2
2,38	4,76	3,57	39,76	29,29	3,1	5,71	4,52	4,76	2,14
0	1,41	2,82	40,35	39,72	4,27	3,27	1,27	3,45	3,45

Table 4.2: Phase Analysis of chosen stable frames, where each row shows the results for a different pullback.

In addition to our in-vivo experiments, we tested our method on in-vitro datasets with ground truths that was mentioned in Section 3.3.1. With known total number of frames, frames per

second and BPM(Beats per minute), we calculated the number of cardiac cycles as:

$$\#cycle = (\#total/fps) * (BPM/60) \tag{4.1}$$

In Table 4.4, number of frames chosen by our algorithm and number of cardiac cycles in pullbacks show agreement. A normalized frame count difference error rate of 0.0769±0.0385 is obtained.

pt_{id}	pb_{id}	#total	$\#ecg$	$\#alg$	length[mm]
1	1	2328	84	87	42.00
1	2	2333	82	75	41.80
2	1	2387	90	84	45.00
2	2	2388	82	73	41.00
2	3	2358	82	75	41.00
2	4	1627	58	57	29.00
2	5	1800	64	59	32.00
3	1	801	27	26	13.50
3	2	2385	94	73	47.00
4	1	2387	90	83	45.00
5	1	2382	91	89	45.50
6	1	2378	90	85	45.00
6	2	2361	80	73	40.00
6	3	2362	90	79	45.00
7	1	2364	89	78	44.50
7	2	2368	95	90	47.50
8	1	2350	83	83	41.50
8	2	2334	90	83	45.00
9	1	2267	80	69	40.00
9	2	2052	69	68	34.50
10	1	2358	84	84	42.00
10	2	988	32	27	16.00
11	1	2383	90	80	45.00
12	1	2379	81	72	40.50
12	2	2358	82	78	41.00

Table 4.3: Comparison of the frame counts chosen by ecg gating algorithm and our image based gating algorithm.pt_{id} is the patient id, pb_{id} is the pullback id, $\#ecg$ represents the number of frames chosen by ecg, $\#alg$ shows the frame count selected by our algorithm and length[mm] is the actual length of the vessel.

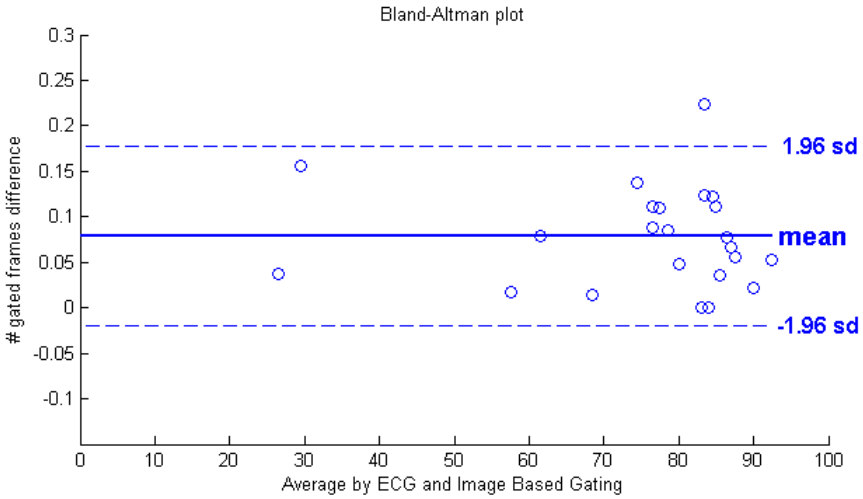

Figure 4.3: Bland-Altmann Analysis of gated frames count calculated by ecg gating and our image-based gating algorithm: 0.0789 ± 0.05.

pb_{id}	$Hertz$	#total	$\#cycle$	$\#alg$
1	1.17	1774	68.99	60
1	1.17	1654	64.32	58
1	1	399	13.3	12
1	1.17	1704	66.27	60
1	1.5	794	39.7	35
1	1.17	1717	66.77	59
1	1.17	755	29.36	28
2	1.17	2494	96.99	100
2	1.17	2547	99.05	92
2	1	2543	84.77	90
2	1.17	2545	98.97	94
2	1.33	2555	113.56	106
3	1	1562	52.07	51
3	1	1161	38.7	40
3	1	1126	37.53	43
3	1	1208	40.27	43
3	1	1185	39.5	40
3	1.17	1129	43.91	42
3	1.33	1204	53.51	47
3	1.5	1190	59.5	53

Table 4.4: Comparison of the frame counts found by our algorithm($\#alg$) and number of cycles($\#cycle$). pb_{id} is the pullback id, $\#total$ represents the total number of frames.

4.3 Comparison With Other Methods

Our method is compared with other state-of-the-art methods available in the literature [13],[10],[11] and PCA[12]. Here, the PCA method will refer to a simpler version of our method with linear dimensionality reduction, i.e. projecting IVUS image frames into 3D vectors using PCA. Some of the current methods [11],[10] for image-based gating do not provide a concrete algorithm for choosing the stable frames but focused more on extracting a 1D Signal. In addition, all the methods in the literature, go through the signal extraction step. Therefore, we base our comparisons on the extracted 1D Signal using a signal to noise measure explained in the following subsection.

4.3.1 Signal to Noise Ratio(SNR) Measure

This measure is first proposed in [10] for in vitro validations. Let us define $Y(\xi)$ as the Fourier transform of our gating signal $y(t)$; the nominal frequency, f_N, as the first harmonic of $Y(\xi)$ and $H(\xi)$, as the filter that is designed to extract the signal and noise from $Y(\xi)$. This can be done by filtering out the signals that are not related to f_N. In Fig. 4.4, an example for $Y(\xi)$ and $H(\xi)$ is shown together. $H(\xi)$ is defined as follows:

$$H_{f_N}(\xi) = \sum_{n=1}^{M} exp\Big(- \frac{(\xi - nf_N)^2}{2\sigma_M^2}\Big) \tag{4.2}$$

The filtered signal is treated as the "actual signal" and the rest of the gating signal is treated as "noise". Thus Signal to Noise Ratio(SNR) is defined as follows:

$$SNR_{dB} = 20log\Big(\frac{\int_\xi |Y(\xi)| H_{f_N}(\xi)}{\int_\xi |Y(\xi)|(1 - H_{f_N}(\xi))}\Big) \tag{4.3}$$

The SNR for methods are shown in Table 4.5. In Fig. 4.5, Box-Whisker plot for SNR values are shown for 5 different methods. The line (in red) inside the box shows the median of SNR values, the box above the median shows the second quartile; while the box below the median shows the third quartile of the SNR values. The black lines show the minimum and maximum values, and the plus signs(in red), denote the outliers. As can be seen in Fig. 4.5 our method(SNR_{alg}) has the best median SNR value, followed by SNR_{pca} and SNR_{mbg}; and only

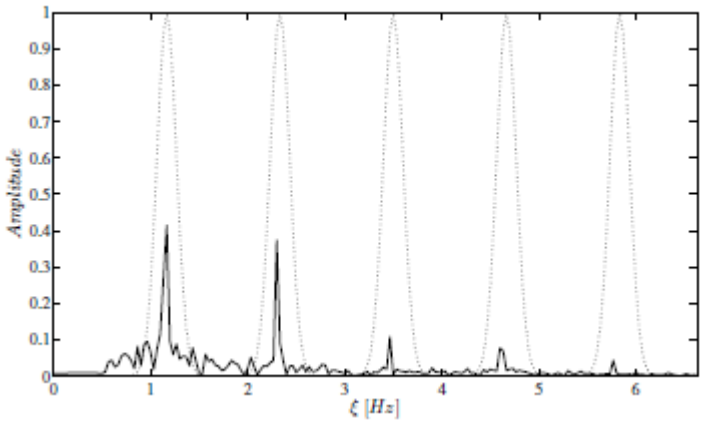

Figure 4.4: $|Y(\xi)|$ and $H_{f_N}(\xi)$ is drawn in solid and dashed lines accordingly, where f_N=1.16 Hz(70 BPM) (taken from [10]).

one outlier, while the others have two outliers. The highest upper median(25%) and maximum value were also produced by our method. The lower median(75%) acquired by the best three methods (*alg* , *pca* and *mbg*) is very close to each other. The only drawback of our algorithm is the variation in the last quartile; the minimum value is lower than the other two methods. However, high median, maximum and high values for the first three quartiles, make our method the best available method and preferable amongst the others.

4.3.2 Qualitative Results

Qualitative results of different methods for 1000 frames are shown in Fig. 4.6. Our and MAL results look visually similar, and seem to preserve the lesion areas that can be seen in nongated pullback longitudinal view. However, in the longitudinal view provided by MBG, dark lesion areas on the bottom-right of the nongated pullback can not be seen anymore.

In addition to the previous methods in literature, we also present a comparison to a primitive method, which would consist of picking frames at regularly spaced intervals for gating. This method, named as the "constant-interval-frame selection" method, is used to demonstrate the performance of our algorithm against a most basic selection criterion.

In Fig. 4.7, the results for constant-interval-frame selection method for two different pullbacks are given. n is chosen as 25,30 and 35, where the frames per second is 30. The gated longitudinal view results for the first pullback do not look similar to ecg gated longitudinal view for any values of n. For the second pullback in the second column, the lumen area of the longitudinal cut for

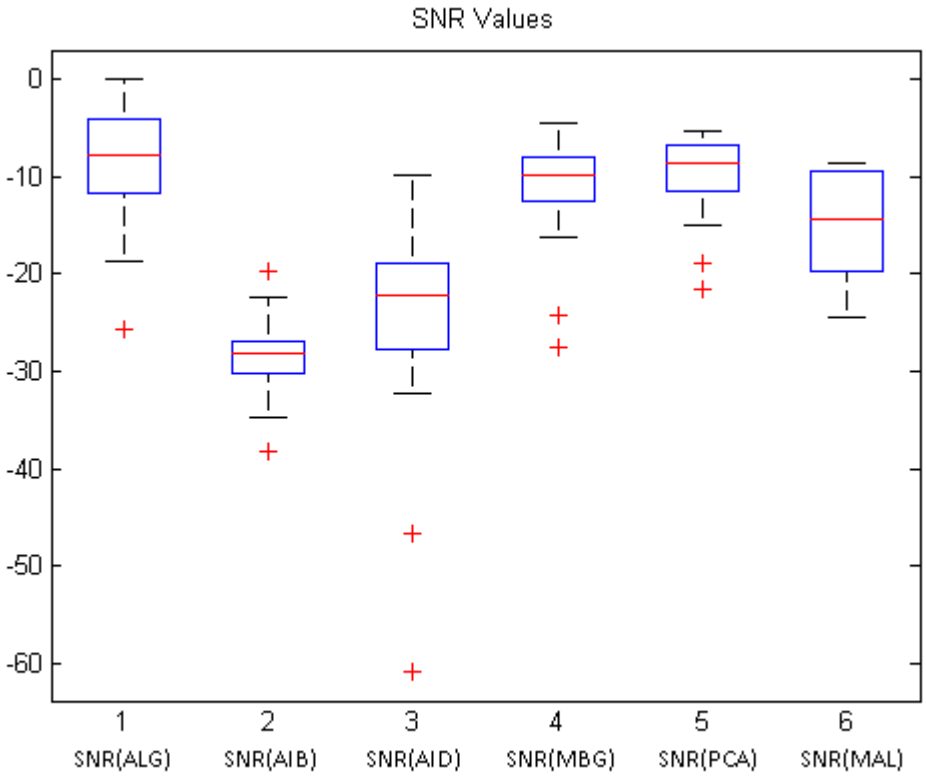

Figure 4.5: Boxplot representation of the SNR Values shown in Table 4.5, ALG: proposed algorithm; AIB:Average Intensity Based[11]; AID: Absolute Difference Based[11]; MBG: Motion Blur Gating[10]; PCA: PCA version of the proposed algorithm[12]; MAL: O'Malley method[13].

pt_{id}	pb_{id}	SNR_{alg}	$SNR_{ibg}(AIB)$	$SNR_{ibg}(AID)$	SNR_{pca}	SNR_{mbg}	SNR_{mal}
1	1	-7.95550	-31.58773	-22.46754	-10.93131	-14.96740	-9.12
1	2	-8.70141	-28.40573	-18.82776	-9.32706	-8.73188	-16.38
2	1	-3.40806	-27.73727	-46.71026	-9.24203	-5.33067	-19.52
2	2	-4.16997	-23.12078	-20.09307	-7.61609	-7.26628	-19.65
2	3	-4.29622	-38.23399	-17.08315	-9.82660	-6.68997	-9.08
2	4	-3.40913	-27.82940	-28.27347	-9.79613	-5.57009	-19.25
2	5	-2.74082	-22.43068	-20.96413	-7.64694	-7.53650	-19.63
3	1	-4.27260	-38.23279	-17.00614	-9.96145	-6.68516	-9.08
3	2	-16.25660	-29.27132	-27.71894	-27.51874	-21.53821	-11.06
4	1	-25.59502	-29.77621	-26.80609	-24.18657	-18.89330	-11.25
5	1	-7.63015	-19.63268	-10.25942	-9.64193	-5.35673	-19.98
6	1	-6.89175	-26.84253	-20.48584	-7.54979	-6.43018	-24.41
6	2	-6.95005	-25.48988	-21.96055	-4.46015	-5.24174	-23.54
6	3	-15.67393	-27.37875	-25.48668	-9.86923	-11.37898	-11.58
7	1	-11.58334	-28.62847	-27.68311	-10.64343	-8.63703	-23.93
7	2	-3.02528	-26.89337	-17.20760	-4.84187	-5.79504	-24.05
8	1	-10.00318	-27.81199	-21.95044	-11.70969	-12.77405	-9.01
8	2	-11.73577	-27.63474	-25.31203	-12.93921	-10.23151	-20.11
9	1	-16.55929	-28.39806	-26.79643	-13.46387	-13.78905	-12.78
9	2	-18.61105	-34.54354	-14.17009	-11.91521	-11.40853	-11.66
10	1	-5.68766	-30.24088	-9.94531	-11.84300	-10.98838	-15.11
10	2	-13.61775	-29.63206	-29.23934	-12.62019	-7.97021	-9.48
11	1	-11.50743	-34.74170	-32.33945	-16.33503	-12.15111	-18.39
11	2	-1.73996	-33.83029	-60.76242	-13.68772	-9.56977	-13.61
12	1	-7.82394	-27.22951	-24.81564	-8.11657	-8.04881	-8.83
12	2	-0.05834	-24.22280	-21.98449	-6.00387	-9.95624	-8.65

Table 4.5: SNR values of our image based gating algorithm(SNR_{alg}); the motion blur algorithm(SNR_{mbg})[10]; the methods in [11], $SNR_{ibg}(AIB)$ for AIB(Average Intensity Based) and $SNR_{ibg}(AID)$ for AID(Absolute Difference Based); Malley method in[13](SNR_{mal}) and PCA(SNR_{pca})[12].

n=25 is similar to those of ecg. However, for different n values the results can dramatically change, thus for the choice of n, one needs to find the average heart rate of the patient that is subject to the pullback. In Fig. 4.8, the results of our image-based gating algorithm versus ecg-gated longitudinal view results are shown for the same pullbacks.

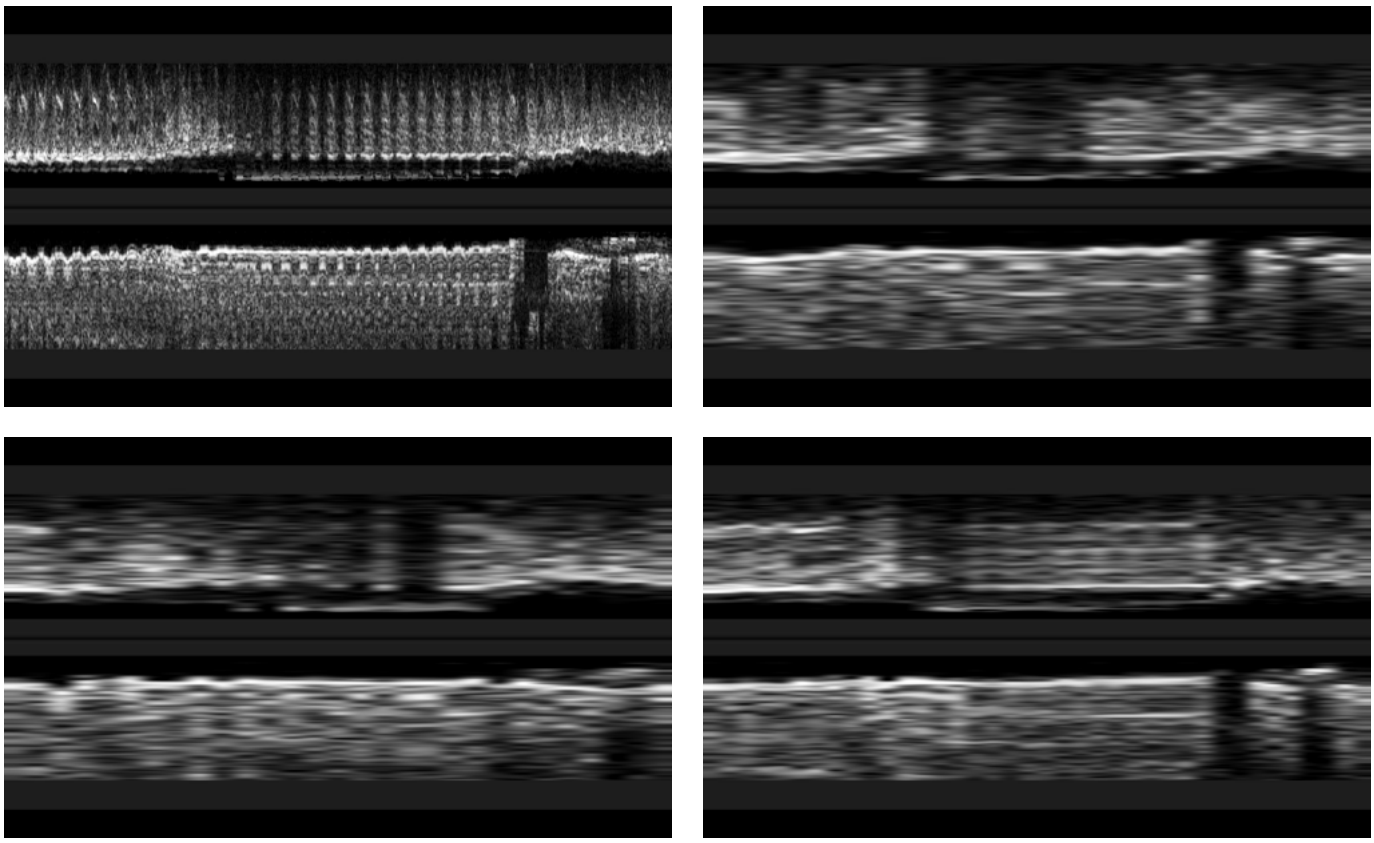

Figure 4.6: *First row;Left* Nongated pullback. *First row;Right* Our gating result.*Second Row; Left:* MBG result *Right:* MAL Results.

4.4 Discussion

In this section, we presented the results of our extensive experiments both on in-vivo and in-vitro datasets. More than 95% of our approximated lumen volume measurements as well as frame count differences showed agreement with those of ECG Gating. The error rate of 0.07% can be explained by manual lumen border detection errors and the cardiac phase difference between ecg and image-based gating. ECG acquires frames that belong to end-diastolic cardiac phase as stated in Chapter 1. Since the frames detected as stable by image-based algorithms may belong to cardiac phases other than end-diastolic the gating results may visually be different, which may cause errors in comparisons of lumen areas. Some sample results are shown in Fig 4.10 and 4.11 for demonstration. Longitudinal IVUS views shown in Fig 4.10, demonstrate similar qualitative outcome for our manifold-learning based IVUS gating method, and the ECG-gated method, which is also verified by the expert cardiologist in the team; and they can be categorized as moderate difficulty pullbacks. However, the pullback in Fig. 4.11, is particularly challenging

due to the big lesion areas present in the arteries and our algorithm and ECG gating produce slightly different results.

The bias in our Bland-Altman analysis of frame count differences may have a few reasons. The first reason is the phase difference that also causes a difference in lumen volume measurements. The second reason is the choice of the patch sizes that is used in section 3.4. If a small number of patch size is chosen, then the number of stable frames may be overestimated; else the number of stable frames may be underestimated.

The running time of our algorithm was 66.32 sec. without any optimization with a Matlab^{TM} *implementa*

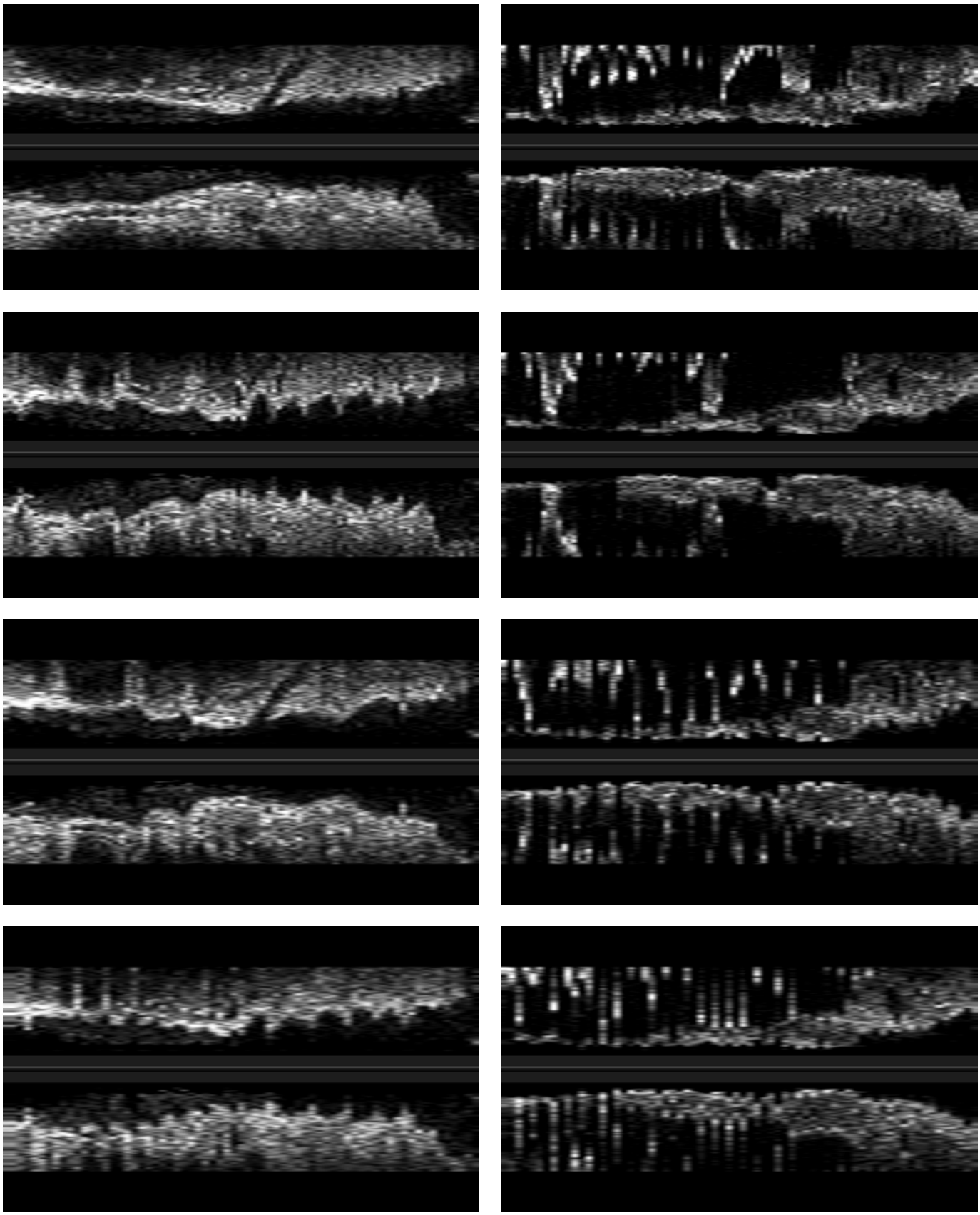

Figure 4.7: *First row;Left* Ecg gated pullback#1. *Second-Third-Fourth Row; Left:* Gating result of pullback#1 for n=25, n=30 and n=35 respectively. *All Rows; Right:* Corresponding results for pullback#2.

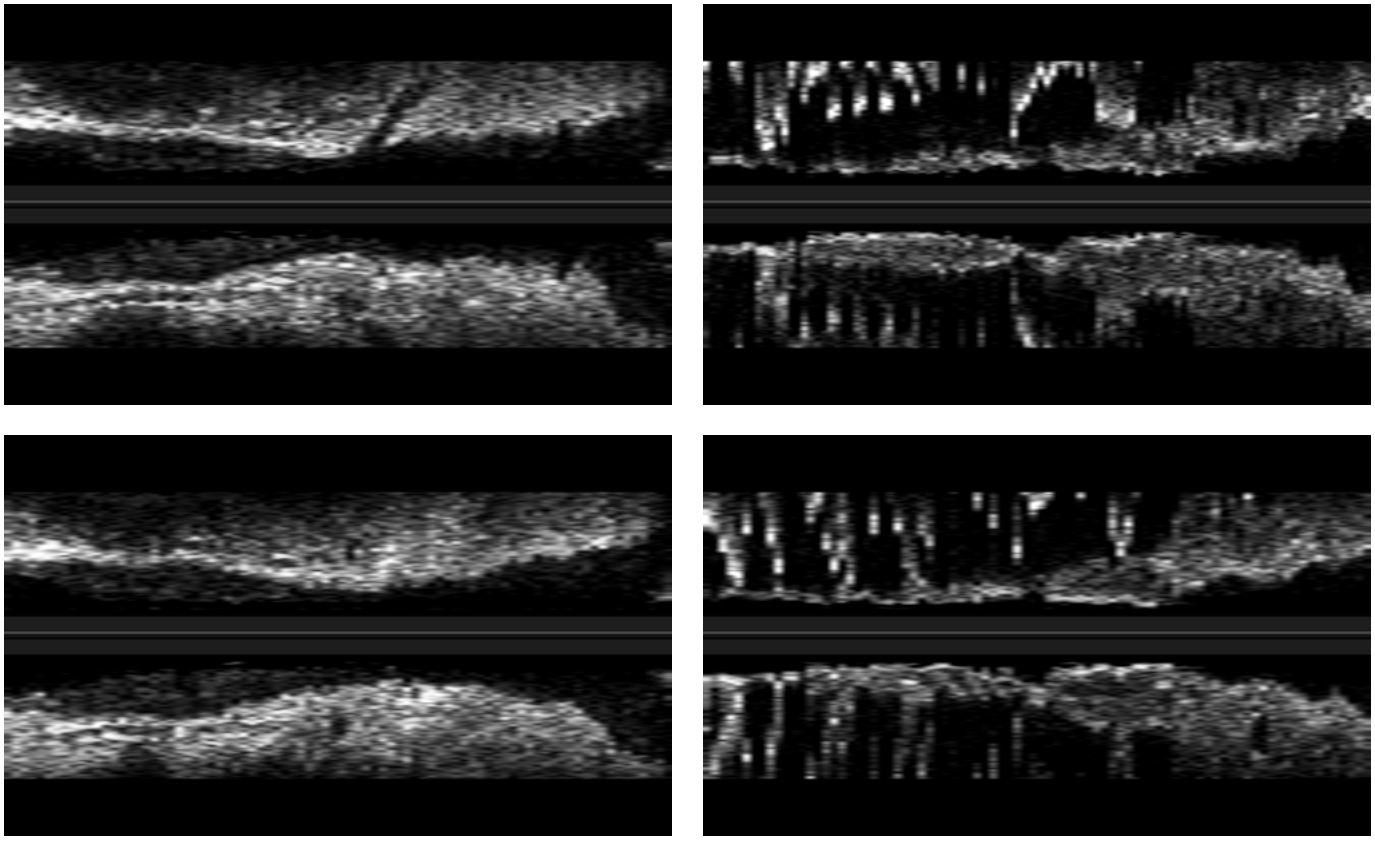

Figure 4.8: *First row; Left* Ecg gated pullback#1. *First row; Right* Ecg gated pullback#2. *Second Row; Left:* Image based gating result of pullback#1. *Second Row; Right:* Image based gating result of pullback#2.

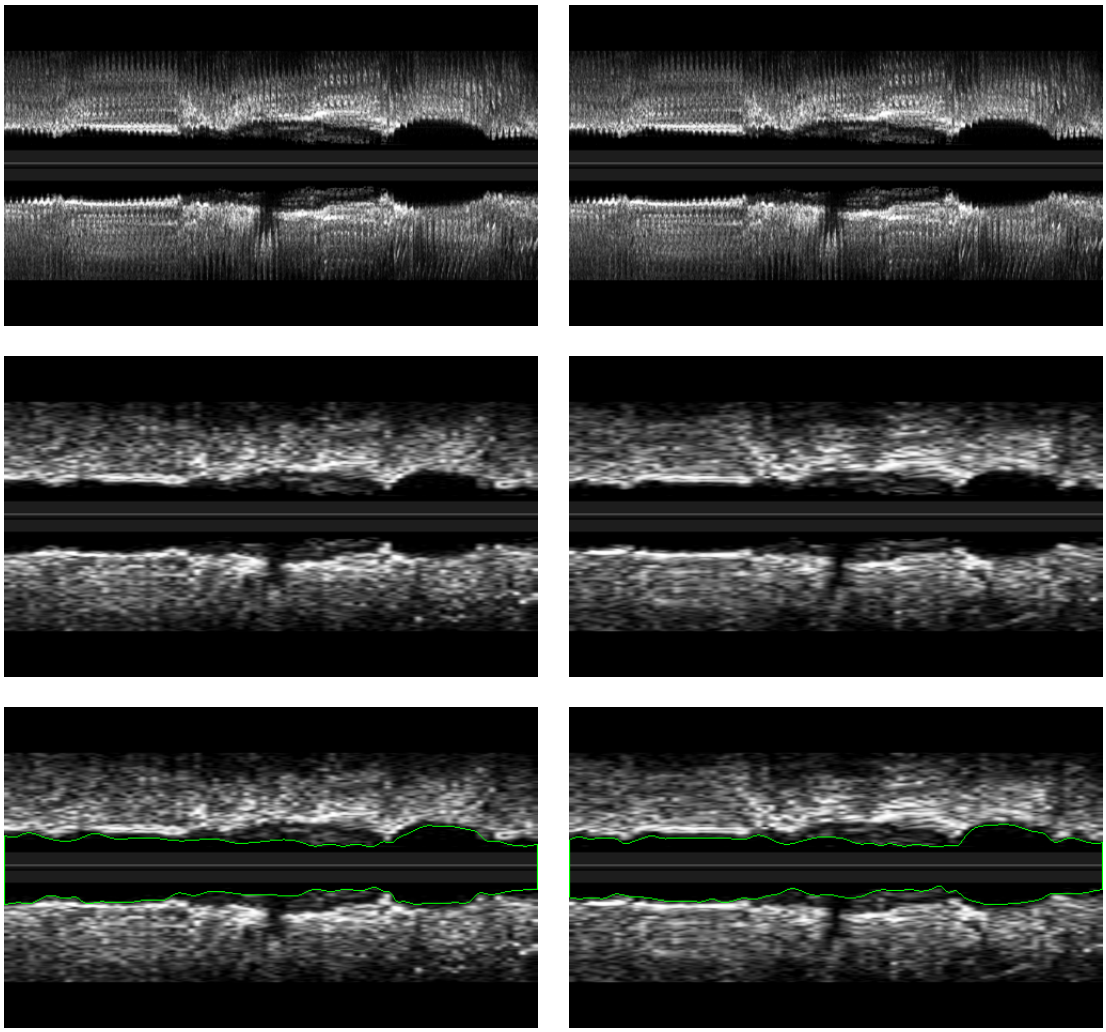

Figure 4.9: *First row:* Nongated pullback. *Middle Row; Left:* Image-based gated pullback. *Right:* Ecg gated pullback. *Bottom Row; Left:* Manual lumen border of image based gated pullback. *Right:* Manual lumen border of ecg gated pullback.

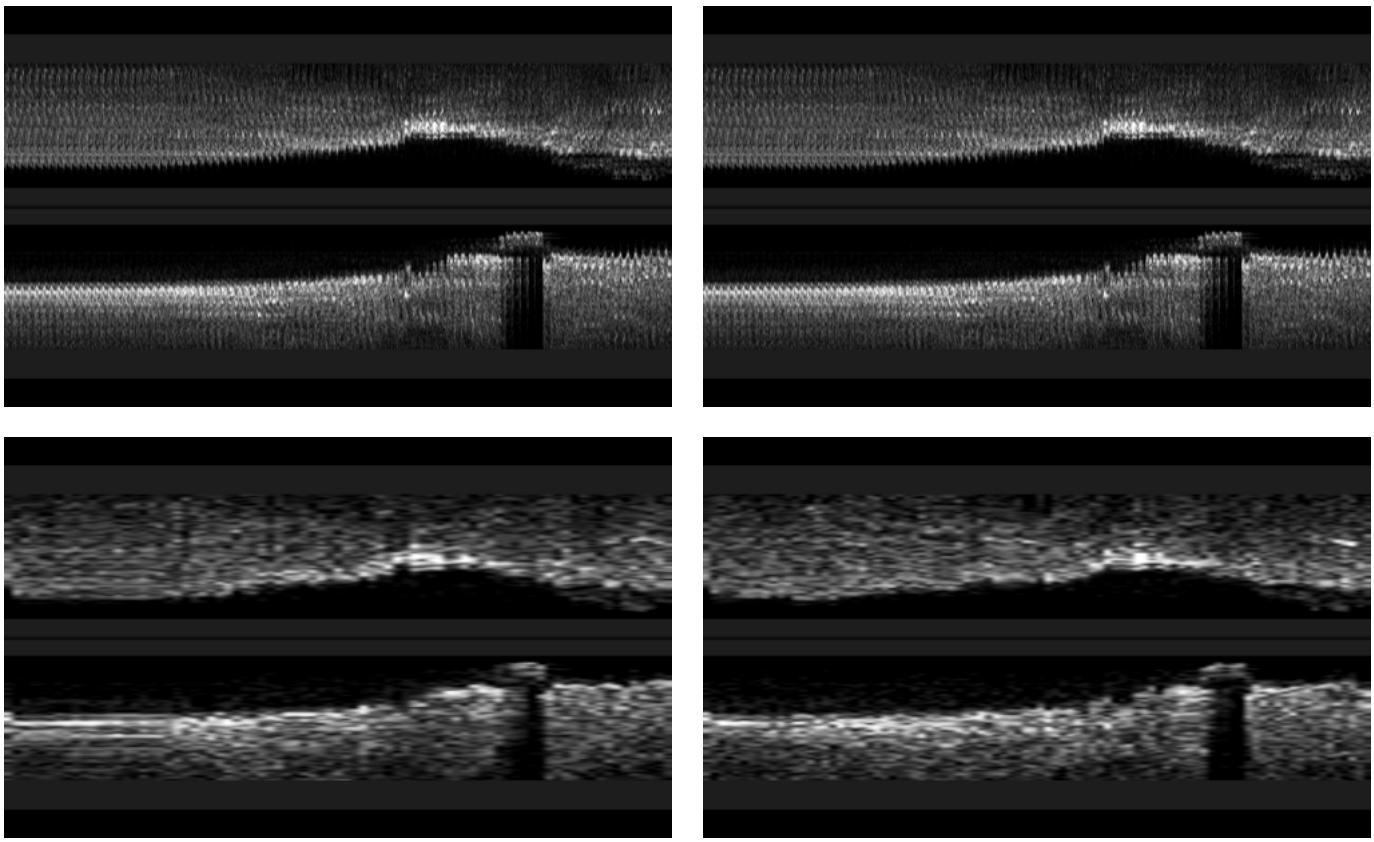

Figure 4.10: *First row:* Nongated pullback. *Middle Row; Left:* Image-based gated pullback. *Right:* Ecg gated pullback.

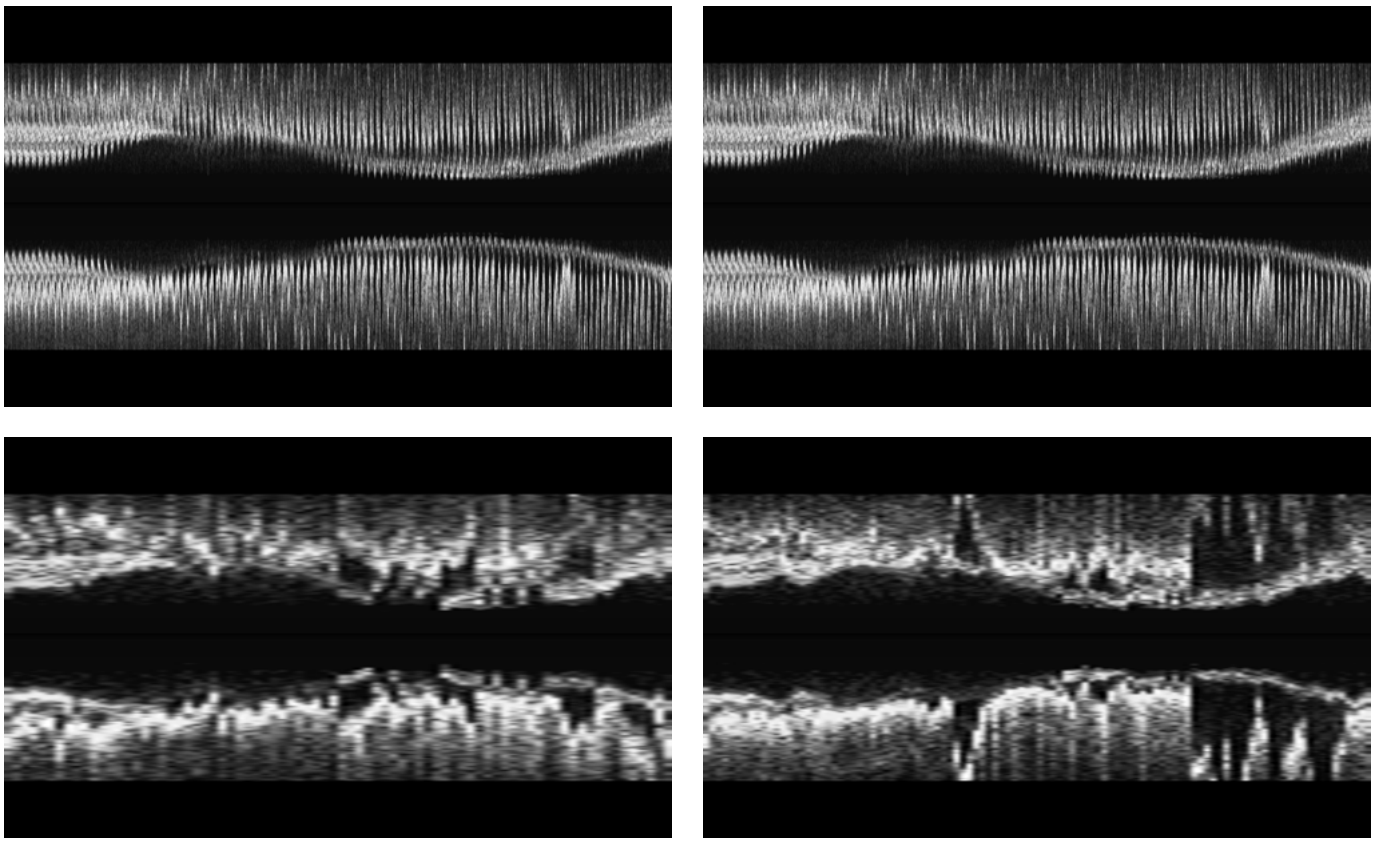

Figure 4.11: *First row:* Nongated pullback. *Second Row; Left:* Image-based gated pullback. *Right:* Ecg gated pullback.

Chapter 5

Conclusions and Future Work

In this thesis, we presented a novel image-based gating method for IVUS sequences. Our method is based on manifold learning, which embeds the similar IVUS frames onto contiguous positions of a low-dimensional manifold lying on a high dimensional image space. Further, we classified the frames by using distances between consecutive eigenvectors that represent the IVUS frames with the help of the frame rate of the pullback and basic heart beat rate knowledge.

In Chapter 1, we introduced the problem definition; the artifacts: morphology change and catheter motion caused by the heart motion; gave an overview of the previous methods and ECG Gating; and stated our contributions. In Chapter 2, we gave an overview of the linear and nonlinear dimensionality reduction techniques that are commonly used in the literature; and detailed information on Laplacian Eigenmaps method. In Chapter 3, we introduced our image-based gating method; a novel similarity measure named Weighted Speckle Distance for ultrasound and presented our in-vitro data experiments for parameter selection; finally we presented the algorithm steps for 1D signal extraction and gating procedure.

In Chapter 4, we tested our method on 12 different patients and 25 different pullbacks. Due to the difficulty of validating in-vivo IVUS data, we introduced a novel way of validation based on lumen area measurements. In the first set of experiments, we validated our method based on approximated lumen volume measurements and frame count differences by comparing the number of selected frames and the lumen areas in 4 different longitudinal views, computed by both methods. Our experiments showed that our method preserves lumen volume $93\% \pm 4$ and our Bland-Altman analysis showed that 95% vessel length is preserved. In the second sets of experiments, we presented extensive comparison results among the existing image-based IVUS gating algorithms available in the literature and PCA as a linear version of our method. Our

experiments showed that our method outperforms all of the methods according to SNR(Signal to Noise Ratio) measure.

Future directions for this work includes;

- Quantitative analysis of lumen area differences from more angles for a better approximation of lumen volume;
- Plaque configuration comparison of the gated pullbacks with ungated pullbacks in order to see the percentage of the important plaques that are preserved after the gating process.
- Applying L1-Minimization of Laplacian Eigenmaps method and comparison with current method.
- Distance mask can be improved: Catheter artifact line can be incorporated to reduce the noise coming from ring-down artifacts and ring-like halo effects around the catheter.
- With a preprocessing of segmentation of the vessel inner and outer wall boundaries, the clusters can be ranked and ordered with respect to the lumen cross section area and the gated frame can be picked according to its lumen area percentage in the cluster.

Bibliography

[1] "What is coronary heart disease," http://criticalillnessexpert.org/kalp-yetmezligi/koroner-arter-hastaligi, Dec 2005.

[2] G. B. Unal, S. Bucher, S. G. Carlier, G. G. Slabaugh, T. Fang, and K. Tanaka, "Shape-driven segmentation of the arterial wall in intravascular ultrasound images," *IEEE Transactions on Information Technology in Biomedicine*, vol. 12, no. 3, pp. 335–347, 2008.

[3] M. Saha, "Scientific basis for design," http://ai.stanford.edu/~mitul/me382/web/spring-reportp6.htm, 2006.

[4] A. Arbab-Zadeh, A. DeMaria, W. Penny, R. Russo, B. Kimura, and V. Bhargava, "Axial movement of the intravascular ultrasound probe during the cardiac cycle: implications for three-dimensional reconstruction and measurements of coronary dimensions." *Am Heart J*, vol. 138, no. 5 Pt 1, pp. 865–72, 1999.

[5] Y. Koren and L. Carmel, "Visualization of labeled data using linear transformations," *IEEE Symposium on Information Visualization*, p. 16, 2003.

[6] S. V. Tenenbaum, J.B. and J. Langford, "A global geometric framework for nonlinear dimensionality reduction ," in *Science*, vol. 290, 2000, p. 2319.

[7] S. T. Roweis and L. K. Saul, "Nonlinear Dimensionality Reduction by Locally Linear Embedding," in *Science*, vol. 290, 2000, pp. 2323–2326.

[8] M. Belkin and P. Niyogi, "Laplacian eigenmaps for dimensionality reduction and data representation," in *Neural Comput.*, vol. 15, 2003.

[9] Todd Wittman, "Manifold learning techniques: So which is the best?" Class on geometric data analysis at University of Minnesota, 2005.

[10] C. Gatta, S. Balocco, F. Ciompi, R. Hemetsberger, O. Rodriguez-Leor, and P. Radeva, "Real-time gating of ivus sequences based on motion blur analysis: Method and quantitative validation." in *MICCAI (2)'10*, 2010, pp. 59–67.

[11] H. Zhu, K. Oakeson, and M. Friedman, "Retrieval of cardiac phase from IVUS sequences," in *Medical Imaging 2003: Ultrasonic Imaging and Signal Processing*, vol. 5035, 2003, pp. 135–146.

[12] I. Jolliffe, *Principal Component Analysis*. Springer Verlag, 1986.

[13] S. M. O'Malley, J. F. Granada, S. G. Carlier, M. Naghavi, and I. A. Kakadiaris, "Image-based gating of intravascular ultrasound pullback sequences," *IEEE Transactions on Information Technology in Biomedicine*, vol. 12, no. 3, pp. 299–306, 2008.

[14] N. Bruining, C. von Birgelen, P. J. de Feyter, J. Ligthart, W. Li, P. W. Serruys, and J. R. Roelandt, "Ecg-gated versus nongated three-dimensional intracoronary ultrasound analysis: implications for volumetric measurements." *Cathet Cardiovasc Diagn*, vol. 43, no. 3, pp. 254–60, 1998.

[15] G. Isguder, G. Unal, M. Groher, N. Navab, A. Kalkan, M. Degertekin, H. Hetterich, and J. Rieber, "Manifold learning for image-based gating of intravascular ultrasound(ivus) pullback sequences," ser. Lecture Notes in Computer Science. Springer Berlin / Heidelberg, 2010, vol. 6326, pp. 139–148.

[16] Robert D. Safian, MD, Mark S. Freed, MD, *Intravascular Ultrasound*. Royal Oak, Michigan: Physicians' Press, 2002.

[17] Aswini Kumar M.D, "Ecg- simplified," http://en.wikipedia.org/wiki/Intravascular_ultrasound, January 2010.

[18] S. de Winter, R. Hamers, M. Degertekin, K. Tanabe, P. Lemos, P. Serruys, J. Roelandt, and N. Bruining, "A novel retrospective gating method for intracoronary ultrasound images based on image properties," in *Computers in Cardiology, 2003*, 2003, pp. 13 – 16.

[19] S. O'Malley, S. Carlier, M. Naghavi, and I. Kakadiaris, "Image-based frame gating of ivus pullbacks: A surrogate for ecg," in *Acoustics, Speech and Signal Processing, 2007. ICASSP 2007. IEEE International Conference on*, vol. 1, 2007, pp. I–433 –I–436.

[20] C. Gatta, O. Pujol, O. Rodriguez-Leor, J. Mauri, and P. Radeva, "Robust image-based ivus pullbacks gating," in *MICCAI (2)*, 2008, pp. 518–525.

[21] Ethem Alpaydin, *Introduction to Machine Learning*. MIT Press, 2004.

[22] Kruskal, J. B., and Wish. M., *Multidimensional Scaling*. Sage Publications, 1977.

[23] I. Fodor, "A survey of dimension reduction techniques," Tech. Rep., 2002.

[24] E. W. Dijkstra, "A note on two problems in connexion with graphs," *Numerische Mathematik*, vol. 1, no. 1, pp. 269–271, December 1959.

[25] A. Schumacher, "Linear and Nonlinear Approaches to the Analysis of R-R Interval Variability," in *Biological Research For Nursing*, vol. 5, 2004, pp. 211–221.

[26] S. C. Malpas, "Neural influences on cardiovascular variability: possibilities and pitfalls," in *Am J Physiol Heart Circ Physiol Vol.*, vol. 282, January 2002, pp. H6–H20.